International Journal of Biological Macromolecules 373 (2026) 153122

Contents lists available at ScienceDirect

International Journal of Biological Macromolecules

journal homepage: www.elsevier.com/locate/ijbiomac

Citric acid-enhanced chitosan/hyaluronic acid interpenetrating hydrogel network as a bioinspired adhesive for osteochondral scaffold fabrication

Mingzu Du [a,*], Giuseppe Tronci [a,b], Xuebin B. Yang [a], Charles Brooker [a,b], David J. Wood [a,c,**]

[a] Biomaterials and Tissue Engineering Research Group, School of Dentistry, University of Leeds, Leeds, LS9 7TF, UK
[b] Clothworkers' Centre for Textile Materials Innovation for Healthcare (CCTMIH), School of Design, University of Leeds, Leeds, LS2 9JT, UK
[c] Bragg Centre for Materials Research, University of Leeds, Leeds, LS2 9JT, UK

ARTICLE INFO

Keywords:
Citric acid
Bioinspired adhesive
Interpenetrating hydrogel network

ABSTRACT

Osteochondral scaffolds often employ multilayered structures to mimic the cartilage–bone interface, but weak interfacial adhesion and insufficient mechanical robustness remain key limitations. To address this challenge, we developed a mussel-inspired interpenetrating hydrogel network (IHN) composed of catechol-functionalised chitosan (Cat–CS) and ultra-high molecular weight methacrylated hyaluronic acid (MeHA) as a bioadhesive phase for osteochondral scaffold fabrication. Leveraging the hydrogen-bonding capability of selected natural polymers, we hypothesised that the acidity of the hydrogel-forming solution could regulate Cat–CS/MeHA network formation, mechanical stability, swelling resistance, adhesion and scaffold bonding. Systematic solvent screening identified citric acid (CA) as the most suitable biocompatible medium, enabling full dissolution of Cat–CS and MeHA and promoting polyelectrolyte complexation (PEC). Increasing CA concentration from 1 to 2 M yielded IHNs with markedly improved macroscopic properties, with Young's modulus increasing from 1.26 ± 0.69 to 7.32 ± 1.84 kPa and swelling ratio decreasing from 359% to 259%. Adhesion strength increased from 0.53 kPa (1 M) to 1.51 kPa (2 M), enabling stable bonding of the hydrogel to a 3D-printed polyhydroxybutyrate (PHB) scaffold after rehydration. Additional cyclic compression, NaOH stability and attenuated total reflection Fourier-transform infrared spectroscopy (ATR–FTIR) analyses were consistent with the formation of a photo-crosslinked MeHA-based IHN reinforced by Cat–CS/MeHA PEC and citrate-mediated secondary interactions. Cytocompatibility assays showed that, after neutralisation, the hydrogels supported fibroblast viability and proliferation over 7 days. Collectively, these findings establish CA-mediated Cat–CS/MeHA IHNs as bioinspired adhesive interfacial layers for integrated osteochondral scaffold fabrication.

1. Introduction

Osteoarthritis (OA) is a common degenerative joint disease that progressively affects the whole joint and severely compromises quality of life [1,2]. Because cartilage and subchondral bone function as an integrated osteochondral unit, effective repair strategies should not only regenerate the cartilage layer but also restore stable integration with the underlying bone-like phase [3,4]. Osteochondral tissue engineering has therefore increasingly focused on bilayered, multilayered and gradient scaffolds that combine soft cartilage-mimicking hydrogels with mechanically supportive bone-like substrates [5–8].

Despite these advances, achieving robust integration between the hydrogel and thermoplastic phases remains a major challenge. Many osteochondral scaffold systems rely on physical assembly or press-fitting between different material layers, which may result in weak interfacial bonding, delamination and unstable load transfer under hydrated and mechanically dynamic conditions [5,9,10]. Therefore, the development of an adhesive hydrogel phase capable of bonding the soft and hard components of osteochondral scaffolds is important for improving construct stability and long-term functional performance.

Mussel-inspired catechol chemistry provides a widely explored route for improving wet adhesion, as catechol groups can participate in hydrogen bonding, metal coordination, π–π interactions and covalent coupling [11,12]. Catechol-functionalised chitosan has therefore

* Corresponding author.
** Correspondence to: D.J. Wood, Biomaterials and Tissue Engineering Research Group, School of Dentistry, University of Leeds, Leeds, LS9 7TF, UK.
E-mail addresses: dnmdu@leeds.ac.uk (M. Du), d.j.wood@leeds.ac.uk (D.J. Wood).

https://doi.org/10.1016/j.ijbiomac.2026.153122
Received 31 March 2026; Received in revised form 10 June 2026; Accepted 18 June 2026
Available online 22 June 2026

attracted attention as a bioadhesive polymer, while chitosan (CS)/hyaluronic acid (HA) systems are also well known to form polyelectrolyte complexes (PECs) through electrostatic interactions between protonated CS and anionic HA [13,14]. In parallel, methacrylated hyaluronic acid hydrogels have been widely investigated as water-stable and cartilage-relevant matrices because HA is an important extracellular matrix component and offers chemical handles for hydrogel design [5]. However, most previous studies have focused on polymer functionalisation, catechol-mediated adhesion, photocrosslinking chemistry or biological performance [13,15,16]. The acidic medium required to dissolve chitosan-based polymers is usually treated as a preparative condition rather than as a design variable that impact secondary interactions and actively determines hydrogel network formation and corresponding macroscopic properties.

This represents an important knowledge gap because acid type and concentration can directly influence chitosan protonation, polymer–polymer complexation, solution homogeneity, ionic interactions and post-gelation stability [13,17]. Acetic acid is commonly used for chitosan dissolution, whereas alternative acid systems, including phosphoric acid and citric acid (CA), have been shown to influence chitosan hydrogel rheology, ionic interactions and network properties [16,17]. Citric acid is of particular interest because it is a naturally occurring multicarboxylic acid with recognised relevance in biomaterials, capable of forming multiple hydrogen-bonding and ionic interactions with polysaccharide chains. Recent reviews have further highlighted citrate-based biomaterials as a versatile class of materials with tuneable structure, biocompatibility, biomimetic viscoelastic behaviour, controllable biodegradation and potential for further functionalisation [9,10]. Nevertheless, its role in regulating secondary molecular interactions and macroscopic properties of interpenetrating hydrogel networks made of catechol-functionalised chitosan and hyaluronic acid (HA) has not been systematically investigated.

Representative studies related to chitosan-HA-based hydrogels are organised in Table 1 according to the adopted material system and design strategy, and whether acid/solvent-mediated network regulation was systematically investigated. These studies have contributed important advances in mussel-inspired adhesion, chitosan modification, HA-based hydrogel formation and citrate-based biomaterials. However, they generally do not address how different acidic solvents regulate the combined dissolution, polyelectrolyte complexation, mechanical reinforcement, swelling resistance and adhesive performance of Cat–CS/MeHA hydrogel networks. In contrast to the aforementioned reports, the present study systematically compares acidic solvents for Cat–CS/MeHA hydrogel formation. (See Fig. 1.)

The aim of this work was therefore to develop a Cat–CS/MeHA interpenetrating hydrogel network (IHN) with solvent-regulated macroscopic properties as a bioinspired adhesive for osteochondral scaffold integration. We hypothesised that citric acid, owing to its multivalent carboxyl groups and hydroxyl functionality, would promote homogeneous polymer dissolution and contribute to network reinforcement through Cat–CS/MeHA polyelectrolyte complexation and citrate-mediated secondary interactions. The effect of acid type and citric acid concentration was evaluated through solubility screening, microstructural analysis, mechanical and rheological testing, swelling assessment, adhesion testing, scaffold bonding evaluation, and cytocompatibility assays. Other than catechol modification and photocrosslinking, the novelty of this work lies in the investigation of citric acid as network-modulating solvent that simultaneously governs Cat–CS/MeHA dissolution, PEC formation, swelling resistance, adhesion and scaffold bonding.

Table 1
Comparison between representative catechol-, chitosan/HA- and citric-acid-based hydrogel studies and the present work.

Representative study	Material system	Novelty	Was acid / solvent effect systematically studied?	Key contributions of present study
Zhao et al. [18]	Chitosan methacrylate / aminoethyl methacrylated HA / catechol-containing chitosan hydrogels	Developed photo-crosslinked and photo-oxidative dual-crosslinked CS/HA/catechol-containing hydrogels with tunable properties by changing polymer functionalisation and network type.	No. The system was prepared in H_3PO_4, but acid type or solvent-mediated effects were not compared.	Directly compares acidic solvents and identifies citric acid as an active solvent-mediated regulator of Cat–CS/MeHA dissolution, PEC formation, mechanical reinforcement, swelling resistance and adhesion.
Conejo-Cuevas et al. [19]	Catechol-modified HA and catechol-modified chitosan	Investigated spontaneous gelation, tissue adhesiveness and film-forming behaviour of catechol-modified polysaccharides.	No. The study focused mainly on catechol oxidation, quinone formation and spontaneous adhesion rather than acid/solvent regulation.	Shifts the focus from catechol-driven gelation alone to solvent-guided Cat–CS/MeHA network formation, with citric acid concentration used to tune hydrogel properties.
Zhou et al. [20]	Catechol-modified chitosan hydrogel	Developed an injectable CS–catechol hydrogel crosslinked by HRP/H_2O_2 for BMSC adhesion and cartilage defect repair.	No. Acid/solvent effects were not systematically investigated.	Addresses a different design question: how acidic solvent type and citric acid concentration control Cat–CS/MeHA hydrogel formation, adhesive performance and scaffold bonding.
Yang et al. [21]	Citric-acid-crosslinked chitosan/gelatin hydrogel loaded with curcumin	Used citric acid as a green crosslinking agent for CS/gelatin hydrogels and evaluated swelling, drug release, degradation, mechanical properties and antibacterial activity.	Partly. Citric acid concentration was varied, but CA was used as a crosslinker in a CS/gelatin drug-delivery system; different acidic solvents were not compared.	Distinguishes citric acid's role as an acidic solvent and network-modulating medium in Cat–CS/MeHA hydrogels, rather than using it only as a chemical crosslinker.
Hamdine et al. [17]	Chitosan hydrogels prepared in phosphoric or oxalic acid	Investigated sol–gel transition and viscoelastic behaviour of acid-based chitosan hydrogels, showing that acid counter-ions and acid type can influence physical gelation.	Yes, but only in chitosan-based physical hydrogels without HA, catechol modification, MeHA photocrosslinking or scaffold bonding.	Extends the concept that acid type matters to a bioadhesive Cat–CS/MeHA interpenetrating hydrogel system and links solvent choice to dissolution, PEC formation, adhesion and osteochondral scaffold integration.
Present study	Cat–CS / UHMW-MeHA interpenetrating hydrogel network	Develops a citric-acid-mediated mussel-inspired adhesive hydrogel combining MeHA photocrosslinking, Cat–CS/MeHA PEC formation and catechol-mediated interactions.	Yes. Acetic acid, hydrochloric acid, phosphoric acid and citric acid are compared, followed by optimisation of citric acid concentration.	Identifies citric acid as an active solvent-mediated network-modulating component that enables homogeneous polymer dissolution, reinforced hydrogel network formation, reduced swelling, improved wet adhesion and persistent bonding to a 3D-printed PHB scaffold.

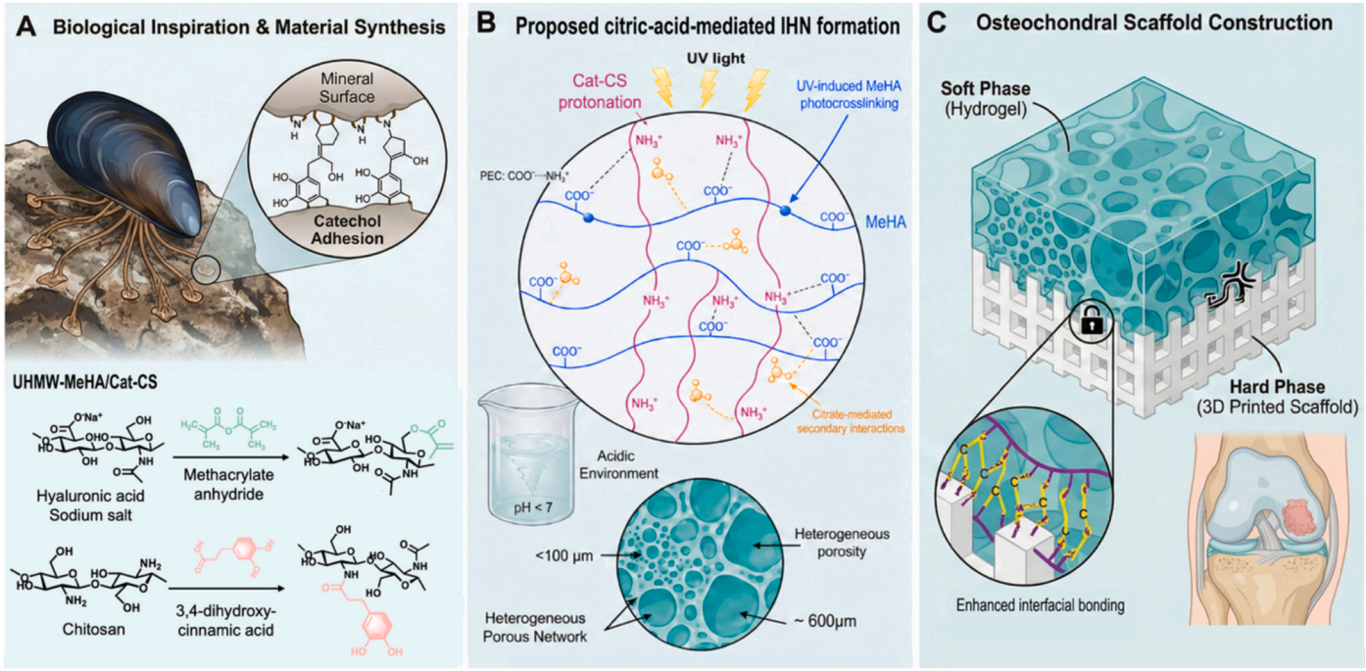

Fig. 1. Mussel-inspired soft-to-hard phase bonding strategy for osteochondral scaffold construction. (A) Schematic illustration of the solvent-mediated design of a bioinspired hydrogel adhesive based on methacrylated hyaluronic acid (MeHA) and catechol-functionalised chitosan (Cat–CS). (B) Proposed citric-acid-mediated interpenetrating hydrogel network (IHN) formation, in which the acidic medium promotes Cat–CS protonation and polymer dissolution, UV exposure induces MeHA photocrosslinking, and polyelectrolyte complexation occurs between COO^- groups on MeHA and NH_3^+ groups on Cat-CS. Citrate species are depicted as non-covalent net-points contributing additional hydrogen-bonding and carboxylate-associated ionic interactions. (C) Integrated osteochondral scaffold featuring enhanced interfacial bonding between the hydrogel and 3D-printed polyhydroxybutyrate (PHB) thermoplastic phase.

2. Materials and methods

2.1. Materials

Hyaluronic acid sodium salt, (m.w. 1.5 MDa) was purchased from BioServ UK Limited. Orthophosphoric acid (85%) was obtained from VWR International. 1-Ethyl-3-(3-dimethylaminopropyl) carbodiimide-HCl (EDC) and sodium nitrite were obtained from Thermo Scientific, UK. Sodium molybdate was purchased from Insight Biotechnology, UK. Dialysis membrane (MWCO: 6–8kD) was purchased from Spectra/Por®, UK. Chitosan (from shrimp shells, ≥ 75% deacetylated), 3,4-dihydroxy-hydrocinnamic acid (DHCA), 2-hydroxy-4′-(2-hydroxyethoxy)-2-methylpropiophenone (I2959), deuterium oxide (D_2O), methacrylic anhydride (MA), citric acid, Dulbecco's modified eagle's medium (DMEM)-high glucose, trypsin, foetal bovine serum (FBS), L-glutamine (LG), penicillin–streptomycin (P/S), modified Giemsa stain, and Cell Counting Kit–8 (CCK-8) were purchased from Sigma-Aldrich, UK. L929 murine fibroblasts were kindly provided by Oral Biology Department, University of Leeds. Phosphate buffered saline (PBS) was purchased from Lonza, UK. Live-or-Dye™ 594/614 Fixable Viability Staining Kit was obtained from Cambridge Bioscience. 4′,6-diamidino-2-phenylindole (DAPI) powder (dilactate) was purchased from Biotium, UK.

2.2. Preparation of cat-CS and UHMW-MeHA

Cat-CS was prepared as previously reported [22]. 0.5 g of chitosan was dissolved in 45 mL of deionised water (pH = 1.6) with vigorous stirring. The pH was adjusted to 5.4 by dropwise addition of 1 M NaOH, and then 591 mg of DHCA was added. 1244 mg of EDC was dissolved in 50 mL of ethanol/water (*v:v* = 50:50) solution and then added dropwise to the previous solution. The final solution was transferred into dialysis tubing (12 kDa MWCO) and dialysed against deionised water (DI H_2O, pH 3–3.5, containing 100 mM of NaCl) for 2 days and then DI H_2O (pH = 5) for 4 h. The final product was obtained *via* freeze-drying.

UHMW-MeHA was produced according to a method adapted from Tran et al. [23]: Hyaluronic acid sodium salt was dissolved in DI H_2O (1 wt%). Methacrylic anhydride was then added dropwise to the solution (1 mL MA per gramme of HA), and the pH of the mixture was kept at 8–11 using 0.5 M sodium hydroxide. The reaction was carried out for 8 h in an ice bath, followed by overnight incubation (at 4 °C). The macromer solution was then purified by dialysis (6–8 kDa) for three days and then freeze-dried.

2.3. Chemical characterisation

Attenuated Total Reflection Fourier Transform Infrared (ATR–FTIR) spectra of the dried polymer samples and air-dried hydrogel samples were obtained using a Spectrum 3 FT-IR spectrometer (PerkinElmer, Waltham, MA, USA) equipped with a Specac Golden Gate™ ATR accessory. Measurements were collected in the range of 4000–600 cm^{-1}, averaging 100 scans for each spectrum. The resolution was set to 4 cm^{-1} with a scanning interval of 2 cm^{-1}. Cured Cat–CS/MeHA hydrogels were analysed by ATR–FTIR either following air-drying or after overnight treatment in 0.5 M NaOH and subsequent air-drying.

Proton nuclear magnetic resonance (^{1}H NMR) spectra were recorded at 298 K on a 500 MHz Bruker Avance Neo spectrometer (Bruker, Billerica, MA, USA) equipped with a DCH helium cryoprobe. Prior to analysis, the sample was dissolved in D_2O to a final concentration of 50 mM at room temperature.

Full UV–Vis absorption spectra of DI H_2O (pH = 2), DHCA, and Cat-CS solution were measured using a microplate reader (Varioskan LUX, Thermo Scientific, Waltham, MA, USA). Measurements were taken in the range of 200–400 nm. DHCA and Cat-CS were dissolved in DI H_2O (pH = 2) at 2 mg/mL prior to analysis.

The Arnow assay test was also applied to further quantify the presence of catechol groups grafted onto the chitosan backbone [24]. Briefly, Cat-CS (n = 3) was first dissolved in 0.5 M HCl at a concentration of 0.0375% (*w/v*). This solution was then mixed with an equal volume of a

combined reagent containing 10% (w/v) sodium molybdate and 10% (w/v) sodium nitrite. After shaking for 5 min, the pH was adjusted to 7.0 using 1 M NaOH. The resulting solution was subsequently brought to a final volume of 5 mL with DI H_2O. A 200 μL aliquot was transferred to a cuvette, and its absorbance was read at 520 nm using a UV–Vis spectrophotometer (Jenway 6350, Jenway, Staffordshire, UK). The degree of substitution (*DS*) was finally calculated by interpolating the absorbance values against a standard curve, as presented in Eq. 1.

$$DS(\%) = \frac{(A - 0.013)\, V\, M_{unit}}{15.97\, M_{cat}\, m_{cs}} \quad (1)$$

A is the measured absorbance values, *V* is the volume of aliquot (0.2 mL), M_{unit} is the average molar mass of chitosan repeat units(171.67 g mol^{-1}, 75% deacetylated), M_{cat} is the molecular weight of DHCA (180.16 g mol^{-1}), and m_{cs} is the mass of Cat-CS samples ($7.5*10^{-5}$ g).

2.4. Solubility test

Due to the sensitivity of the chitosan chains to the type of counterion (*i.e.*, the acid ions), various acids such as DI H_2O (pH = 2), phosphoric acid, acetic acid, citric acid, and hydrochloric acid were evaluated as potential solvents. Two optimisation rounds were performed. Initially, the acid concentration was kept constant (1 M) and different component ratios (Cat-CS: MeHA = 3/10, 10/10, 15/15, 20/20 mg/mL) were applied. Subsequently, the component ratio was kept constant (3/10), and a concentration range of 0.5-2 M of different acids was applied. The solubility was scored as fully dissolved, partially dissolved or insoluble.

2.5. Preparation of hydrogels

The solvents were first prepared by mixing the indicated acid with 1% (*w/v*) I2959 at a 7:3 ratio at 37 °C. Subsequently, Cat-CS and MeHA were dissolved at final concentrations of 3 and 10 mg/mL, respectively. The resulting precursor solution was transferred to a 24-well plate and centrifuged at 3000 rpm for 5 min. The plate was then exposed to UV light for 20 min on each side.

2.6. Scanning electron microscope (SEM)

A Hitachi SU5000 SEM (Hitachi High-Tech, Tokyo, Japan) equipped with a field emission electron source and a secondary electron detector was used in this study. The instrument was operated at an acceleration voltage of 5 kV under high vacuum conditions. All hydrogel samples were freeze-dried and then fractured in liquid nitrogen. Specimens were then mounted on 15 mm diameter stubs using conductive tape and sputter-coated with gold for 40 s in an Agar Auto Sputter Coater prior to imaging.

2.7. Mechanical and rheological tests

Freshly prepared hydrogels (Ø: 16 mm, h: 8 ± 1 mm, $n = 3$) were subjected to unconfined compression testing at a rate of 3 mm min^{-1} using a mechanical testing system equipped with a 10 N load cell (ELF 3200, Bose Corporation, Eden Prairie, MN, USA). The compressive modulus was determined by linear fitting of the stress–strain curve within the 10–15% strain range. Rehydrated samples were prepared by air-drying the cured hydrogels and incubating them in 0.5 M NaOH solution overnight [25,26]. The same compression protocol was subsequently performed to evaluate the mechanical behaviour after alkaline treatment.

Cyclic compression testing was further performed on freshly prepared hydrogels to evaluate their short-term cyclic mechanical response, energy dissipation and recoverability. Hydrogel specimens with comparable geometry to those used for monotonic compression were placed between two parallel compression platens without preload. Testing was conducted in displacement-controlled mode up to 30% compression for 10 consecutive loading–unloading cycles at 0.1 Hz. The displacement amplitude was calculated individually from the measured initial height of each specimen, and force–displacement data were recorded for analysis.

Engineering compressive strain was calculated as displacement divided by the initial specimen height, while compressive stress was calculated as force divided by the initial cross-sectional area. Cycle 2 was used as the reference cycle for quantitative comparison to minimise the influence of initial sample seating and contact adjustment during the first loading cycle. Dissipated energy was calculated by numerical integration of the area enclosed by the loading–unloading stress–strain hysteresis loop. As strain is dimensionless, integration of stress with respect to strain gives an energy density. The calculated dissipated energy was converted and reported as J/m^3.

Peak compressive stress was defined as the maximum compressive stress reached during cycle 2 and was reported in kPa.

Stress retention after 10 cycles was calculated using Eq. 2 as the percentage of peak compressive stress maintained after repeated cyclic compression and was used to indirectly quantify short-term hydrogel recoverability:

$$\text{Stress retention}\ (\%) = \left(\frac{\sigma_{10}}{\sigma_2}\right) \times 100\% \quad (2)$$

where σ_2 and σ_{10} are the peak compressive stresses measured during cycles 2 and 10, respectively.

Rheological characterisation was performed to assess the viscoelastic and shear-thinning behaviour of freshly cured hydrogels (Ø: 25 mm, $n = 4$) using an MCR 301 rheometer (Anton Paar, Graz, Austria) [27]. An amplitude sweep was first carried out at an angular frequency of 10 rad·s^{-1} to identify the linear viscoelastic region, followed by frequency sweeps at room temperature with a constant strain amplitude of 1%. A steady shear test was performed to record the viscosity as a function of shear rate. The shear rate was swept from 0.01 to 1000 s^{-1} in a logarithmic ramp mode. At each shear rate point, the measurement was conducted under steady-state conditions with an equilibration time of 10 s to ensure equilibrium before data acquisition.

2.8. Swelling test

Swelling behaviour was evaluated by immersing the dry specimens in 1.5 mL of PBS (10 mM, pH 7.4) at 37 °C for 24 h, in line with previous publications [28–30]. The initial dry weight (m_0) and the swollen equilibrium weight (m_s) of each sample were measured, and the swelling ratio (*SR*, $n = 3$) was determined according to Eq. 3:

$$SR = \frac{m_s - m_0}{m_0} \times 100\% \quad (3)$$

2.9. Adhesion test

Fresh porcine skin was cut into rectangular pieces (6 × 2 cm) and carefully defatted. A 1 mL aliquot of precursor solution was applied to a 2 × 2 cm overlapping region and UV-cured for 20 min using a UV cabinet (C-71, Analytik Jena, Jena, Germany) equipped with four 15 W 365 nm tubes. The light intensity at the working surface (measured using a photometer at the sample position) was 2000 μW cm^{-2}, and the samples were positioned approximately 10–12 cm from the UV source. Adhesion tensile testing was performed using an Instron universal testing machine (5544, Instron, Norwood, MA, USA) at a crosshead speed of 10 mm min^{-1}, and adhesion strength was calculated by dividing the peak force by the bonded area [31,32]. All tests were performed in triplicate ($n = 3$). LIQUIBAND® served as the commercial control.

For the adhesion demonstration, freshly cured hydrogels were immersed in 0.5 M NaOH overnight for neutralisation, air-dried, and subsequently rehydrated in PBS overnight prior to evaluation.

2.10. Cytotoxicity test

L929 murine fibroblasts were cultured in T-75 flasks containing high-glucose DMEM supplemented with 10% FBS, 1% LG, and 1% P/S at 37 °C in a humidified atmosphere of 5% (*v/v*) CO_2. All incubations were performed under identical conditions unless otherwise specified.

Direct contact cytotoxicity testing was conducted in accordance with ISO 10993-5:2009(E). Freshly cured and rehydrated hydrogel samples ($n = 3$) were placed and fixed in six-well plates and washed twice with PBS. Subsequently, cell culture medium containing 5×10^4 cells per well was added, and the plates were incubated for 96 h. After incubation, the cells were washed twice with PBS and fixed with neutral-buffered formalin for 15 min and then stained with 20% Giemsa solution for 20 min and examined under a Leica DM16000 B inverted microscope for imaging.

Indirect cytotoxicity testing was performed using material extracts. Briefly, rehydrated hydrogel samples ($n = 3$) were placed in six-well plates, and 5 mL of culture medium was added to each well. After 24 h incubation, the extracts were collected and stored at 4 °C. Following this, 100 μL of cell suspension was seeded into a 96-well plate (5000 cells per well) and incubated for 24 h. Then, 10 μL of material extract was added to each well, and the plates were further incubated for 1, 3, and 5 days. At each time point, 10 μL of CCK-8 solution was added to each well and incubated for 1 h. The absorbance at 450 nm was measured using a microplate reader.

Live/Dead Staining: Cells were seeded into 60 mm × 15 mm petri dishes at a density of 5×10^4 cells per dish. After 24 h, the culture medium was replaced with media containing the material extracts, and cells were cultured for 1, 3, 5, and 7 days. At each time point, Live-or-Dye™ 594/614 dye (1:100 in PBS) was added and incubated for 30 min at room temperature. After washing with PBS, cells were fixed with 4% paraformaldehyde for 15 min and permeabilised with 0.1% Triton X-100 for 10 min. Cells were then stained with DAPI (1 μg/mL) for 10 min. Images were acquired using a confocal laser scanning microscope (CLSM, Leica TCS SP8). A positive control was prepared by adding ethanol to a final concentration of 15% and incubating for 10 min.

2.11. Statistical analysis

Data normality was assessed using OriginPro 2025 (OriginLab Corporation, USA). Statistical differences were evaluated using one-way ANOVA followed by Tukey's post-hoc test. A *p*-value of less than 0.05 was considered statistically significant. Data were presented as mean ± standard deviation (SD).

3. Results and discussion

3.1. Chemical characterisation of HA and CS derivatives

The successful synthesis and chemical modification of MeHA and Cat-CS were confirmed by FTIR and ^{1}H NMR spectroscopy. In the FTIR spectra (Fig. 2A–E), native HA (A) exhibited characteristic absorption bands at 1610 cm^{-1} and 1036 cm^{-1}, corresponding to the C═O stretching of the amide and the C–O–C groups, respectively. After methacrylation (B), new signals appeared near 1720 cm^{-1} corresponding to the characteristic C═O ester bond (carbonyl stretch) of the methacrylate groups, together with a slightly higher signal intensity at 950 cm^{-1} corresponding to = C–H bond formation [33]. DHCA (D) showed strong signals at 1660 cm^{-1} and 1439 cm^{-1} associated with aromatic C═O and carboxylic O—H stretching, which overlap with the FTIR signals of native CS (C) [34]. However, in catechol–chitosan (E), the emergence of aromatic and phenolic–OH stretching bands between 3200 and 3500 cm^{-1}, together with the C═O stretching and N – H bending vibrations of newly formed amide bonds formed at 1740 and 1600 cm^{-1}, demonstrated the successful EDC-mediated coupling of DHCA onto the chitosan backbone through amide bond formation [22].

The ^{1}H NMR spectra (Fig. 3A-D) further verified these chemical modifications. For MeHA (B), new vinyl proton peaks appeared at 5.7 and 6.2 ppm, confirming the presence of methacrylate residues [35–37]. Based on the ratio of the integrated vinyl proton signals to the combined methyl protons of the *N*-acetyl group in HA ($\delta \sim 1.9$ ppm), the degree of methacrylation of HA was calculated to be approximately 59% [38]. The DHCA spectrum (C) displayed aromatic proton signals between 6.5 and 7.0 ppm, whereas catechol–chitosan (D) exhibited additional aromatic resonances in this region, indicating the successful incorporation of catechol groups. Based on the ratio of the integrated areas to the reference chitosan signal at δ 2.06 ppm (CH_3) and assuming three aromatic protons per catechol group, the degree of substitution was calculated as 27.4%. This result indicates that approximately 27 mol% of the chitosan repeating units were grafted with catechol groups [39]. Collectively, these FTIR and NMR results therefore confirmed the successful synthesis of MeHA and Cat-CS.

Additional confirmation of these chemical modifications was obtained *via* UV–Vis spectrophotometry. Fig. 4(A) presents the UV–Vis absorption spectra of different samples. The black curve corresponded to deionised water at pH 2, showing no distinct absorption features in the visible range. The red curve, assigned to DHCA, exhibited a characteristic absorption peak around 280 nm, indicative of the phenolic hydroxyl and conjugated aromatic structures [40]. In contrast, the catechol–chitosan (blue curve) displayed a broader and slightly red-shifted band, confirming the successful grafting of catechol moieties onto the chitosan backbone. In addition, no absorption above 300 nm confirmed that Cat-CS remained in a non-oxidised state.

Fig. 4(B) demonstrates the colorimetric responses obtained from the Arnow assay. The catechol–chitosan solution initially appeared pale white under acidic conditions (0.5 M HCl), turning yellow upon sequential addition of sodium nitrite and sodium molybdate, and then turning intense red under 1 M NaOH, confirming the presence of catechol groups. This occurred as hydrogen ions from the phenolic hydroxyl groups reacted with nitrite ions to produce nitroso derivatives of the

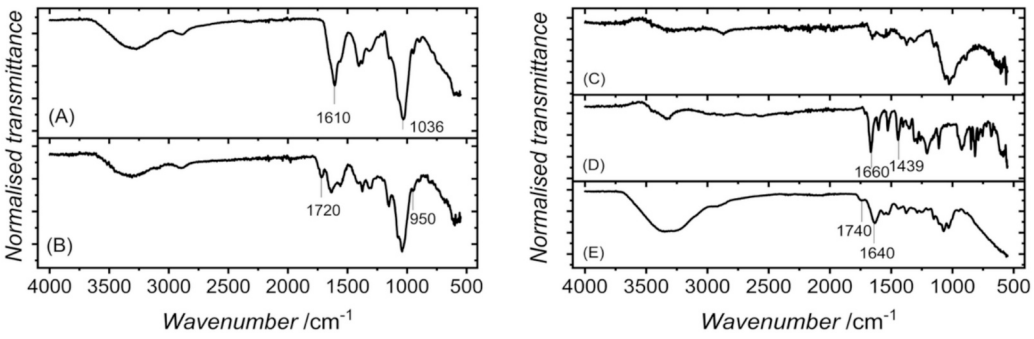

Fig. 2. FTIR analysis of synthesised materials. FTIR spectra of HA (A), MeHA (B), CS (C), DHCA (D), and Cat–CS (E). The characteristic absorption bands are consistent with methacrylation of HA and catechol modification of CS.

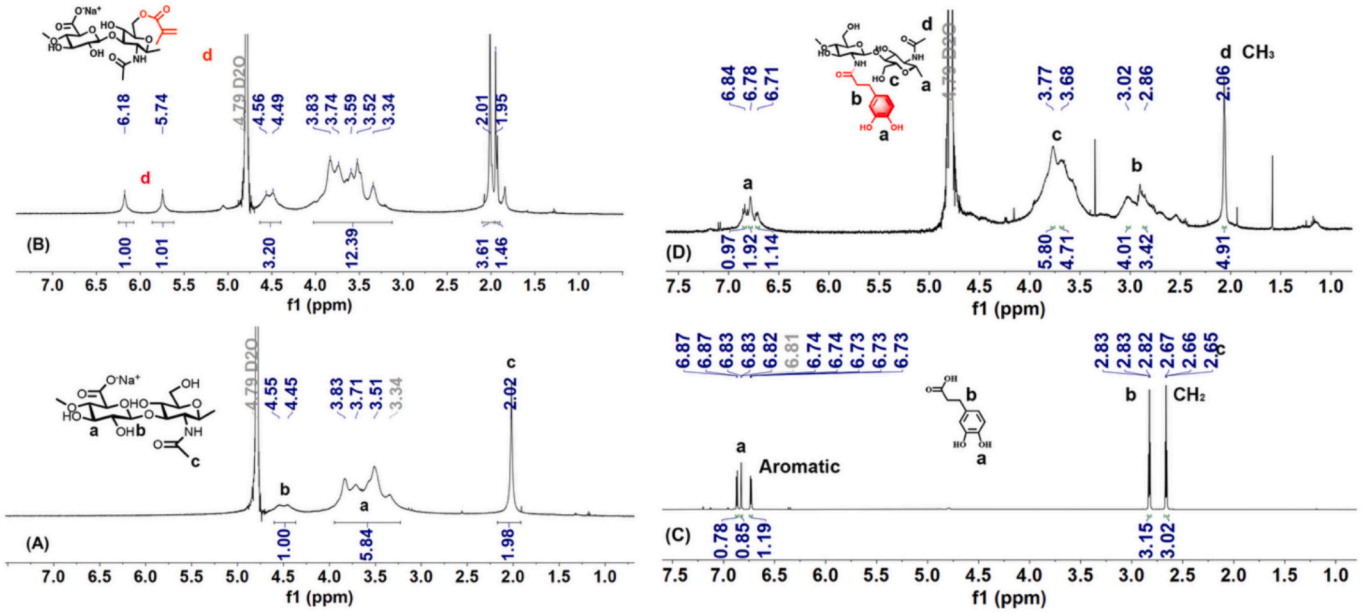

Fig. 3. ^{1}H NMR analysis of synthesised materials. ^{1}H NMR spectra of HA (A), MeHA (B), DHCA (C), and Cat–CS (D). The characteristic methacrylate and aromatic proton signals are consistent with the chemical modification of HA and CS, respectively.

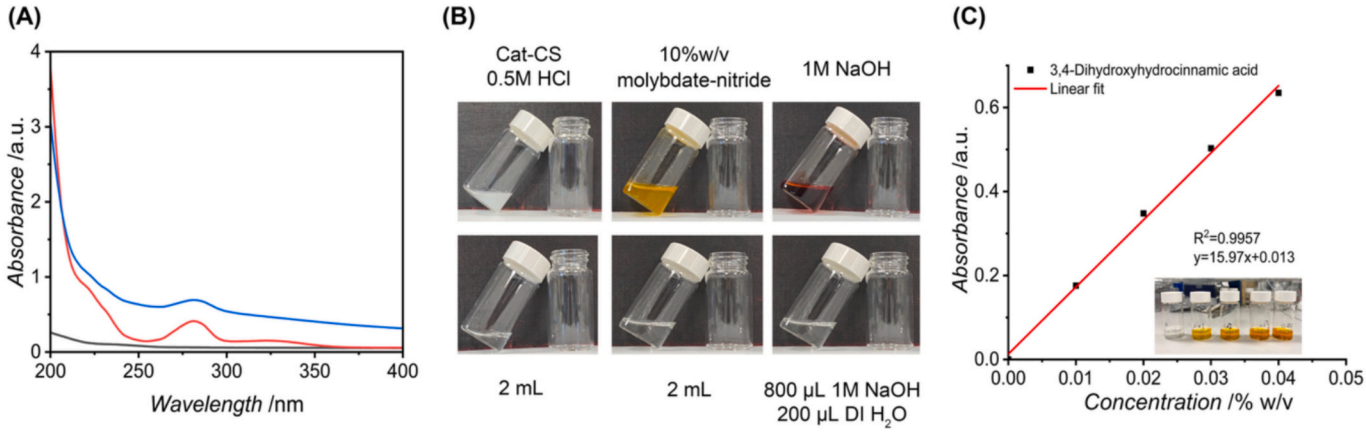

Fig. 4. UV–Vis characterisation and catechol quantification. (A) UV–Vis spectra of DI H_2O (pH 2, black), DHCA (red), and Cat–CS (blue) showing the red-shifted, broadened absorption band characteristic of catechol conjugation. (B) Arnow assay colourimetric responses comparing DI H_2O (bottom) with Cat–CS in 0.5 M HCl (top). (C) Calibration curve of caffeic acid ($R^2 = 0.997$) used for catechol quantification.

phenols, resulting in colour formation. Sodium molybdate stabilised the intermediate nitrous acid formed during the reaction, preventing its rapid decomposition [41]. Hence, the progressive colour changes from yellow to orange and finally to red visually validate the formation of the catechol–molybdate complex under alkaline conditions.

Fig. 4 (C) shows the calibration curve established using DHCA as a standard. The absorbance intensity at the characteristic wavelength increased linearly with concentration ($R^2 = 0.997$), verifying excellent correlation and analytical reliability. The inset photographs illustrated the corresponding colour gradient with increasing standard concentration. This standard curve was subsequently applied to quantify the catechol content in the synthesised catechol–chitosan conjugates.

Table 2 summarises the quantification of catechol grafting in Cat–CS samples as determined by the Arnow assay. The OD values were measured at the characteristic wavelength of the catechol–molybdate complex and converted to DS using the caffeic acid calibration curve. All samples, prepared at the same concentration (0.0375% *w/v*), exhibited OD values in the range of 0.125–0.147, corresponding to DS values between 17.8% and 21.3%. The relatively consistent DS among replicates indicated good reproducibility of the conjugation process and confirmed the effective grafting of catechol groups onto the chitosan backbone.

Table 2
Quantification of catechol grafting in Cat–CS samples using the Arnow assay. The degree of substitution was calculated from the OD values based on the caffeic acid calibration curve.

Sample ID	Concentration of Cat-CS / %*w/v*	OD Value	*DS* / %
1	0.0375	0.125	17.8
2	0.0375	0.147	21.3
3	0.0375	0.134	19.2

However, the DS obtained from ^{1}H NMR analysis (27.4%) was slightly higher than that calculated from the Arnow assay (≈19%). This difference was attributed to the distinct measurement principles of the two methods. The NMR technique directly quantified the integrated signal ratio of catechol aromatic protons to the reference chitosan peaks, reflecting the total number of grafted catechol units. In contrast, the

Arnow assay detected only phenolic hydroxyl groups that remained chemically accessible and capable of forming complexes with molybdate under alkaline conditions. Partial oxidation of catechol groups during synthesis or their involvement in intra- or intermolecular hydrogen bonding, may have reduced the number of reactive phenolic sites, leading to a lower apparent DS value from the colorimetric method [42,43]. Overall, both analyses consistently confirmed the successful functionalisation of chitosan with catechol moieties, with the NMR-derived value representing the theoretical total substitution and the Arnow assay the effective reactive catechol content.

3.2. Optimisation of solubility and internal porous structure

Solubility tests revealed clear differences in the behaviour of Cat–CS/MeHA mixtures across the four acidic media (Fig. 5). In Optimisation (A), hydrochloric acid was the only solvent that consistently produced clear, fully dissolved solutions at all polymer ratios, indicating effective protonation of chitosan and good disruption of the polymer network. Citric acid performed reasonably well at lower concentrations: the 3–10 mg/mL sample dissolved completely, but increasing the polymer content led to visible undissolved material. This trend was also evident in the photographs of the four citric-acid samples. When the vials were slightly tilted, the 3–10 mixture showed the greatest mobility and flowed readily, whereas mobility decreased progressively in the 10–10, 15–15 and 20–20 formulations. The reduced flowability reflected the gradual transition from a homogeneous solution to partially dissolved or nearly insoluble mixtures. By comparison, phosphoric acid dissolved only the lowest-concentration samples and was largely ineffective at higher polymer loadings, while acetic acid also failed to fully dissolve the mixtures across all concentration combinations.

Optimisation (B) further highlighted the clear solvent-dependent differences in polymer dissolution. Hydrochloric acid dissolved all formulations across the tested molarity range (0.5–2 M), indicating effective protonation of chitosan. Citric acid showed a strong concentration effect: the polymers remained insoluble in 0.5 M solution but became fully dissolved when the molarity increased to 1 M or above. In contrast, the mixtures remained insoluble in acetic acid at all tested concentrations. Phosphoric acid was only effective at 0.5 M and failed to dissolve the polymers at higher concentrations. As expected, the pH ≈ 2 DI H_2O control did not promote dissolution, confirming that acidity alone was insufficient and that specific interactions between the acids and the polymer chains were required to achieve full solubilisation.

Although hydrochloric acid demonstrated superior solubilising performance across the tested concentrations, it was not selected for subsequent hydrogel evaluation because it is a strong mineral acid and its corrosive nature raises concerns for downstream cell-based studies. By contrast, phosphoric acid and citric acid are generally recognised as safe (GRAS) by the U.S. Food and Drug Administration, making them more appropriate for biomaterial formulation and subsequent biological testing [44,45].

As phosphoric-acid-based hydrogels underwent severe oxidation during freeze-drying and could not be reliably imaged, the SEM analysis focused on hydrogels prepared using citric acid. The SEM images (Fig. 6) revealed a highly porous, interconnected network, although the pore structure varied noticeably across the sample. The left-hand region (B) displayed a comparatively compact architecture with smaller, more closely distributed pores, whereas the right-hand region (A) contained much larger, more open pore domains. Quantitative pore size analysis

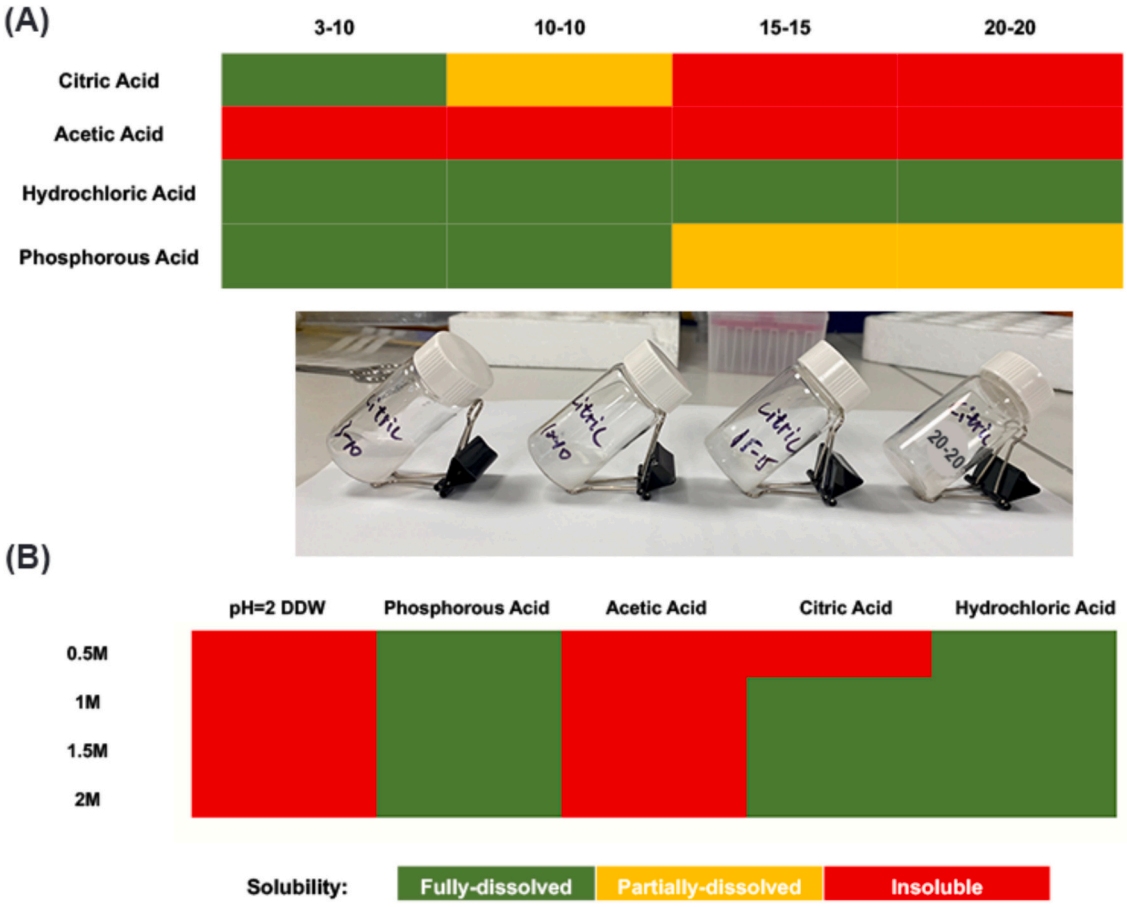

Fig. 5. Solubility screening of Cat–CS/MeHA mixtures under different acidic conditions. (A) Polymer ratio optimisation in four acids. (B) Concentration-dependent dissolution and flowability. Colours correspond to solubility states indicated in the legend.

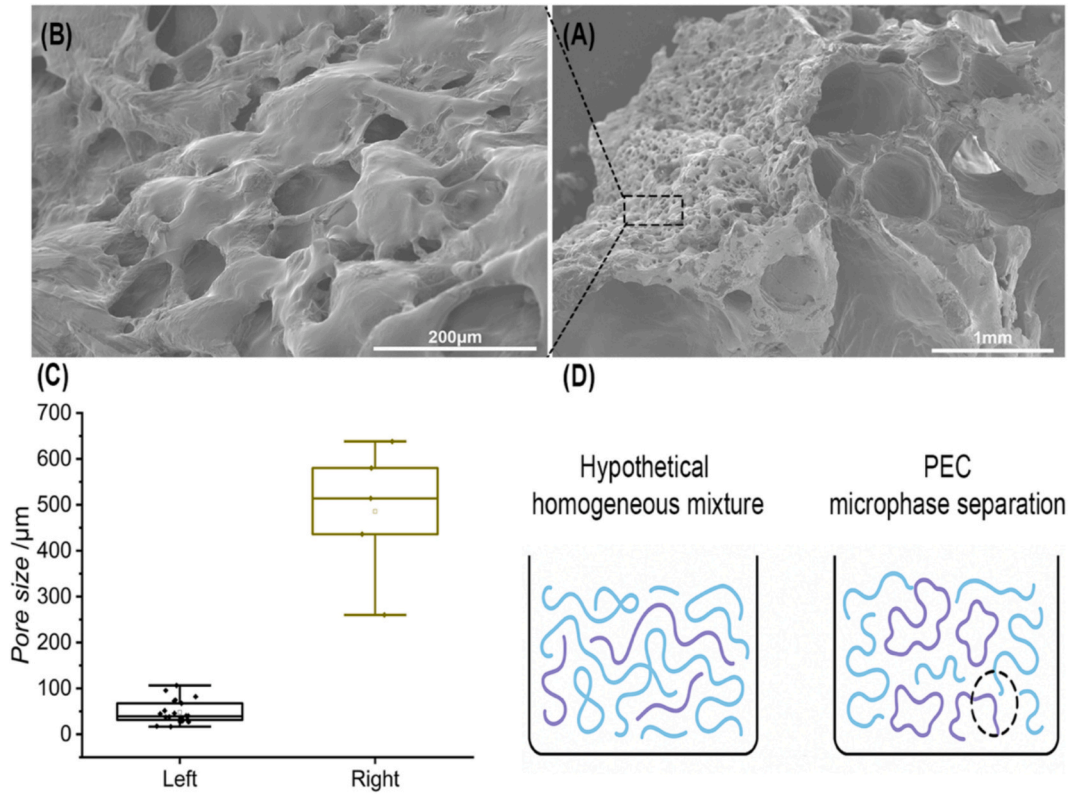

Fig. 6. Microstructural characterisation of citric-acid-processed Cat–CS/MeHA hydrogels. (A) Low-magnification SEM image showing heterogeneous pore distribution. (B) High-magnification view of the region highlighted in (A). (C) Quantification of pore size across left and right sample regions. (D) Schematic contrasting homogeneous polymer mixing with microphase separation arising from polyelectrolyte complex (PEC) formation.

supported this observation (C): the left region exhibited a narrow distribution with most pores falling below approximately 100 μm, while the right region showed a substantially wider spread, with median pore sizes exceeding 400 μm and individual pores reaching nearly 600 μm. This clear separation between tightly packed and more open domains underscores the presence of intrinsic structural heterogeneity within the hydrogel.

Such differences are consistent with microphase separation during PEC formation (D). As illustrated schematically, a perfectly homogeneous mixture would be expected to produce a uniform pore network, while PEC-related segregation can generate domains with differing polymer densities, giving rise to the contrasting structures observed here.

In the subsequent experiments, the polymer composition was fixed at 3–10 mg/mL to reduce variability arising from changes in polymer ratio. This allowed the study to focus specifically on how different concentrations of citric acid influenced the organisation of the hydrogel network. Phosphoric acid, which has been reported in the literature as a solvent for chitosan-based systems [17], was included as a reference condition to provide a comparative baseline. After preparing and imaging hydrogels dissolved in the three citric acid concentrations, all samples consistently exhibited the same region-dependent pore disparity illustrated in Fig. S1. This recurrent pattern suggests that the heterogeneous pore distribution is intrinsic to the Cat–CS/MeHA system under citric-acid–based dissolution conditions rather than an isolated anomaly.

Additionally, these distinct regional variations in pore architecture may provide functional benefits for cartilage regeneration. The smaller pores (<100 μm) identified on one side of the structure are likely to enhance mechanical stability against compressive deformation, helping to maintain the load-bearing requirements of cartilage tissue [46]. These confined pores may also delay fluid diffusion and matrix degradation, contributing to long-term structural retention at the cartilage surface where mechanical stress is highest [47]. In contrast, the larger pores approaching ~600 μm promote rapid fluid exchange and permit efficient cell ingress, facilitating early cell colonisation and matrix deposition in deeper regions of the construct [48,49]. Such multi-scale porosity can support both mechanical function and biological integration, providing a microenvironment conducive to chondrocyte survival, nutrient transport and tissue maturation [50,51]. Consequently, this intrinsic heterogeneity may be advantageous for osteochondral repair, offering a potentially useful structural gradient for future osteochondral scaffold design.

3.3. Mechanical and rheological behaviour of hydrogels

The stress–strain curves (Fig. 7A) demonstrated clear solvent-dependent mechanical differences. The 2 M citric-acid hydrogel showed the highest compressive resistance, whereas the 0.5 M phosphoric acid hydrogel ranked second, outperforming the more compliant 1 M and 1.5 M citric-acid groups. This trend aligned with the Young's modulus values (Fig. 7B), where the 2 M citric-acid hydrogel reached 7.32 ± 1.84 kPa compared with 3.63 ± 1.05 kPa for phosphoric acid, while the 1 M and 1.5 M samples remained markedly lower (1.26 ± 0.69 and 1.50 ± 1.55 kPa, respectively), supporting a concentration-dependent reinforcement effect.

The rheological results further supported this interpretation (Fig. 7C–D). Although the H_3PO_4-treated hydrogel exhibited the highest reduction in shear modulus (G′: ~108 ➔ ~51 Pa) during frequency sweep, it also showed the most drastic viscosity (η) drop from 459.11 Pa·s to 0.005 Pa·s when shear rate was increased from 0.01 to 1000 s^{-1}, indicating a brittle and easily disrupted network. By contrast, the 2 M citric acid-treated hydrogel presented a more controlled variation in viscoelastic properties (G′: 68 ➔ 33 Pa; η: 403 ➔ 0.004 Pa·s) and

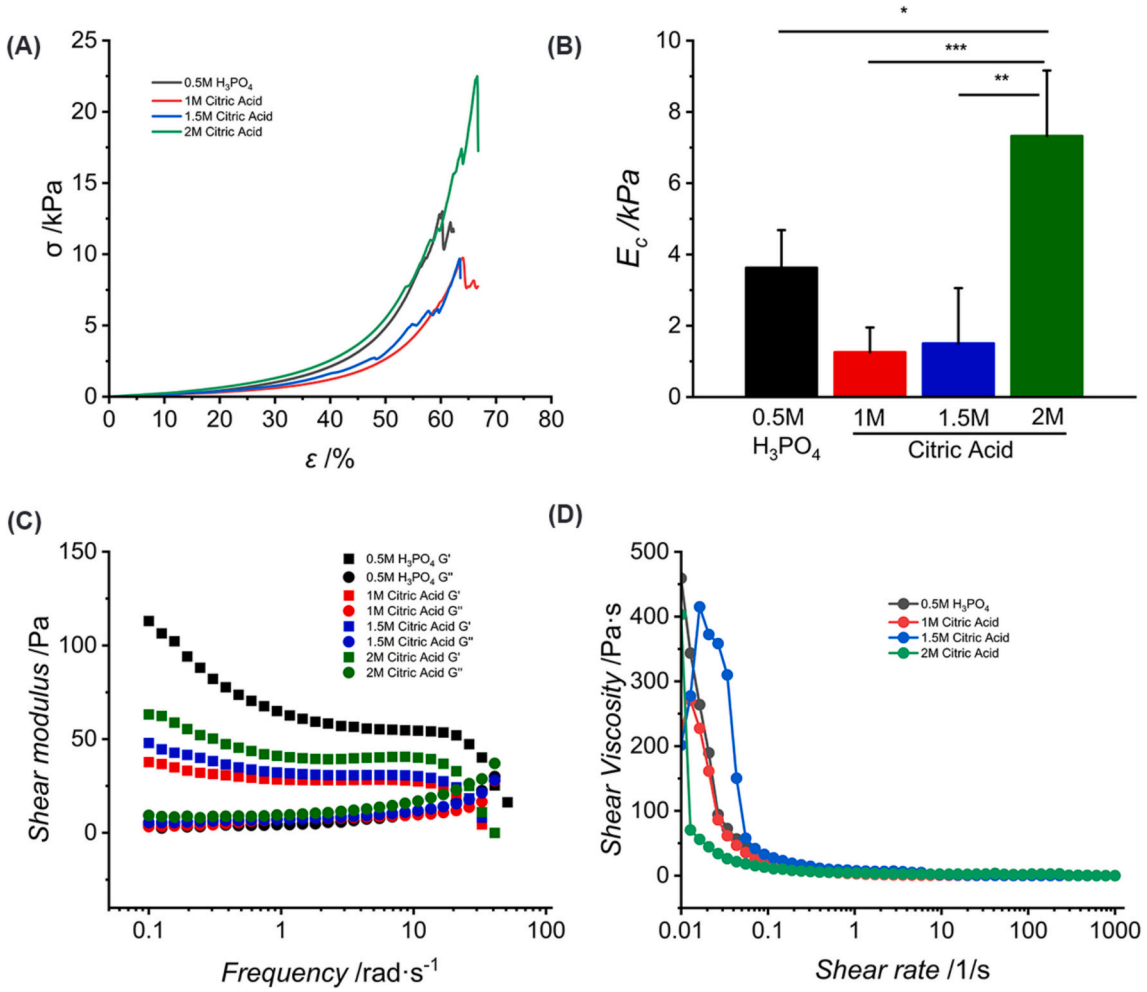

Fig. 7. Mechanical and viscoelastic properties of hydrogels prepared with phosphoric acid and increasing concentrations of citric acid. (A) Representative compression stress–strain curves; (B) Young's modulus, with statistical differences indicated by asterisks; (C) Storage modulus (G′) and loss modulus (G″) obtained from frequency sweep; (D) Shear viscosity as a function of shear rate. Colour coding and symbol definitions are provided within the figure panels.

enhanced structural integrity during the same measurements. The 1 M and 1.5 M groups again demonstrated the weakest resistance to flow-induced breakdown.

Together, these results suggest two distinct acid-mediated network behaviours: phosphate-associated ionic aggregation, which produced comparatively unstable structures under deformation, and citrate-mediated polyelectrolyte/secondary interactions, which promoted a more cohesive Cat–CS/MeHA network capable of resisting shear forces. Here, "citrate-mediated" refers to hydrogen-bonding and carboxylate-associated ionic interactions; no metal–ligand coordination mechanism was introduced or investigated in the present formulation. The enhanced mechanical resilience of the 2 M citric-acid hydrogel under hydrated conditions may therefore be advantageous for cartilage and osteochondral applications, where hydrogels must withstand cyclic joint loading, resist swelling-induced displacement, and maintain intimate adhesion to surrounding tissues to ensure effective defect sealing and stable biological integration.

While the monotonic compression and rheological tests demonstrated solvent-dependent differences in stiffness and flow resistance, these measurements do not fully describe the response of hydrogels under repeated loading. To further evaluate the cyclic mechanical response of freshly prepared hydrogels, cyclic compression tests were performed at 30% compressive strain for 10 cycles. As the hydrogel component is intended to function as the soft cartilage-like phase within a biphasic osteochondral scaffold, its ability to tolerate repeated compressive deformation is an important consideration beyond monotonic compressive strength. Representative compression stress–strain hysteresis loops at cycles 2 and 10 are shown in Fig. 8A, with full cyclic loop profiles at cycles 1, 2, 5 and 10 provided in Supplementary Fig. S2. Cycle 2 was selected as the reference cycle for quantitative comparison to minimise the influence of initial sample seating and contact adjustment during the first loading cycle. All hydrogel groups exhibited repeatable loading–unloading curves, indicating that the hydrogel networks were able to withstand repeated compression without obvious mechanical collapse.

The dissipated energy, calculated from the area enclosed by the hysteresis loop, was used to assess cyclic energy dissipation during repeated compression. The dissipated energy at cycle 2 was 13.7 ± 3.7 J/m^3 for the 0.5 M H_3PO_4 group, 14.4 ± 7.5 J/m^3 for the 1 M citric acid group, 16.9 ± 4.5 J/m^3 for the 1.5 M citric acid group and 34.0 ± 18.5 J/m^3 for the 2 M citric acid group. Although the 2 M citric acid group showed the highest mean dissipated energy at cycle 2, no statistically significant difference was detected among the groups (Fig. 8B).

Stress retention after 10 cycles was calculated as $\sigma_{10}/\sigma_2 \times 100\%$, where σ_2 and σ_{10} represent the peak compressive stress at cycles 2 and 10, respectively. All groups maintained high stress retention after repeated compression, with values of 98.89 ± 1.59% for the 0.5 M H_3PO_4 group, 98.42 ± 1.79% for the 1 M citric acid group, 98.35 ± 0.83% for the 1.5 M citric acid group and 98.03 ± 1.07% for the 2 M citric acid group (Fig. 8C). These results demonstrate a predominantly

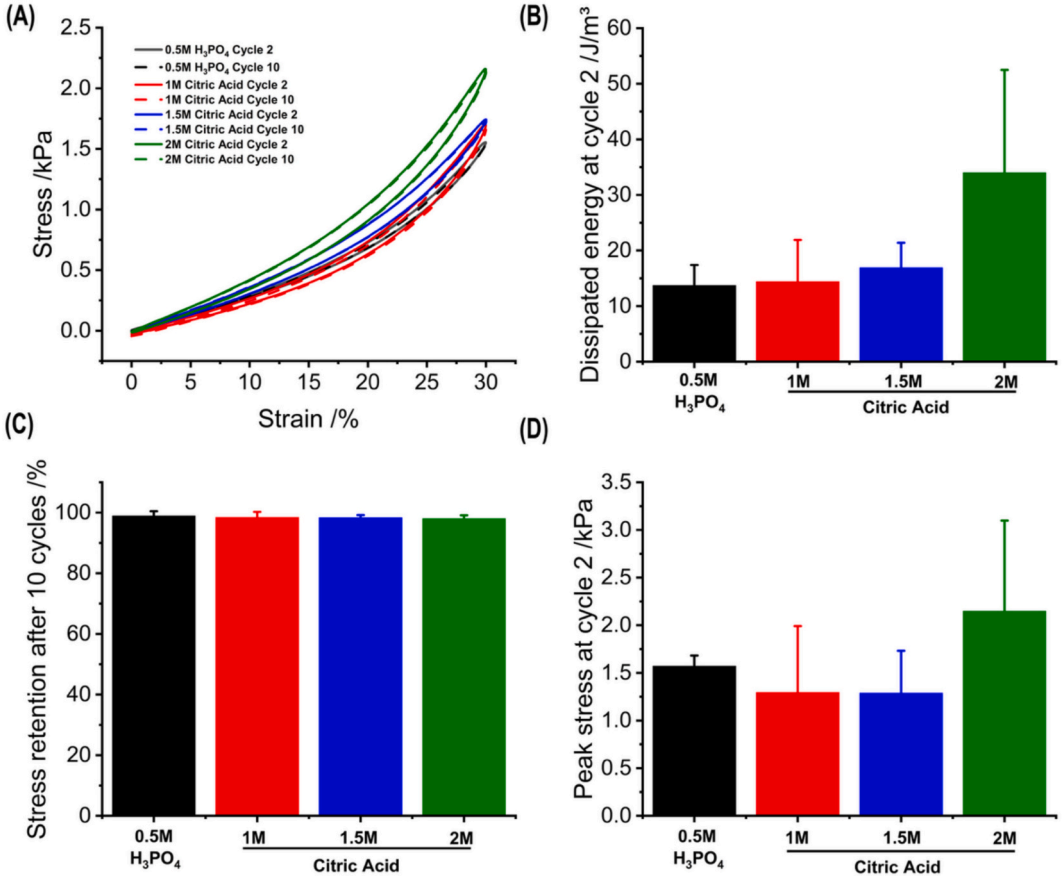

Fig. 8. Cyclic compression behaviour of hydrogels prepared using phosphoric acid or citric acid. (A) Representative cyclic compression stress–strain loops at cycle 2 and cycle 10 under 30% compressive strain. (B) Dissipated energy at cycle 2, calculated from the area enclosed by the loading–unloading hysteresis loop. (C) Stress retention after 10 cycles, calculated as $\sigma_{10}/\sigma_2 \times 100\%$, where σ_2 and σ_{10} represent the peak compressive stress at cycle 2 and cycle 10, respectively. (D) Peak compressive stress at cycle 2. Data are presented as mean ± SD.

elastic behaviour with significant short-term cyclic recoverability up to 10 compression cycles at 30% compression.

The peak stress at cycle 2 was 1.571 ± 0.111 kPa for the 0.5 M H_3PO_4 group, 1.295 ± 0.697 kPa for the 1 M citric acid group, 1.287 ± 0.444 kPa for the 1.5 M citric acid group and 2.148 ± 0.951 kPa for the 2 M citric acid group. The 2 M citric acid group showed the highest mean peak stress at cycle 2, although the difference was not statistically significant (Fig. 8D). Overall, these cyclic compression results provide additional mechanical indicators beyond monotonic compression, including cyclic energy dissipation and short-term recoverability, and support the short-term cyclic mechanical stability of the citric-acid-mediated hydrogel networks as soft adhesive phases for osteochondral scaffold fabrication.

3.4. *Swelling behaviour and tissue adhesion performance*

Fig. 9A shows the swelling behaviour of hydrogels prepared using different acidic solvents. After 24 h of immersion in PBS, the 0.5 M phosphoric acid hydrogel exhibited the highest swelling ratio at 381%, followed by the 1 M citric-acid formulation at 359%. In contrast, the 1.5 M and 2 M citric-acid hydrogels showed substantially reduced swelling, reaching only 222% and 259%, respectively. These reductions are consistent with enhanced carboxylate-associated ionic interactions within the photo-crosslinked MeHA-based network, which limited water uptake [52]. The greater swelling observed for the H_3PO_4-based gel suggested a more loosely organised structure capable of accommodating higher levels of hydration.

Fig. 9B illustrates the force–displacement behaviours of the hydrogels adhered to porcine skin. The light grey LIQUIBAND® curve (in terms of the left purple y axis) exhibited the steepest loading slope and the highest peak force before failure, reflecting strong and rapid interfacial bonding. In contrast, the grey MeHA-only hydrogel (right orange y axis) showed an early failure with a shallow force gradient compared to LIQUIBAND®, consistent with weak adhesion in the absence of catechol groups. Among the experimental hydrogels, the black curve (0.5 M phosphoric acid) and the green curve (2 M citric acid) demonstrated more sustained loading and delayed failure, indicating greater mechanical resistance. The red curve (1 M citric acid) showed the poorest performance in this regard, whereas the blue curve (1.5 M citric acid) provided intermediate resistance to displacement.

Fig. 9C summarises the tensile adhesion strength of each formulation on porcine skin, and the results agreed well with the behaviours observed in the force–displacement curves. LIQUIBAND® showed the highest bonding strength (10.84 ± 0.59 kPa), as expected from a clinical-grade adhesive. The CS-free hydrogel displayed poor adhesion (0.85 ± 0.14 kPa), indicating that the presence of catechol residues in the resulting network was key to ensuring interfacial fixation. The 0.5 M H_3PO_4 hydrogel achieved 1.57 ± 0.18 kPa, confirming the contribution of ionic interaction to adhesion enhancement. For citric acid-based hydrogels, the lowest value was observed in the 1 M group (0.53 ± 0.23 kPa), suggesting insufficient PEC formation at this acidity. However, increasing citric acid concentration led to a noticeable improvement: the 1.5 M and 2 M groups reached 1.27 ± 0.15 kPa and 1.51 ± 0.04 kPa, respectively. These strengths were consistently higher than MeHA control and approached the level obtained with the phosphoric-acid formulation.

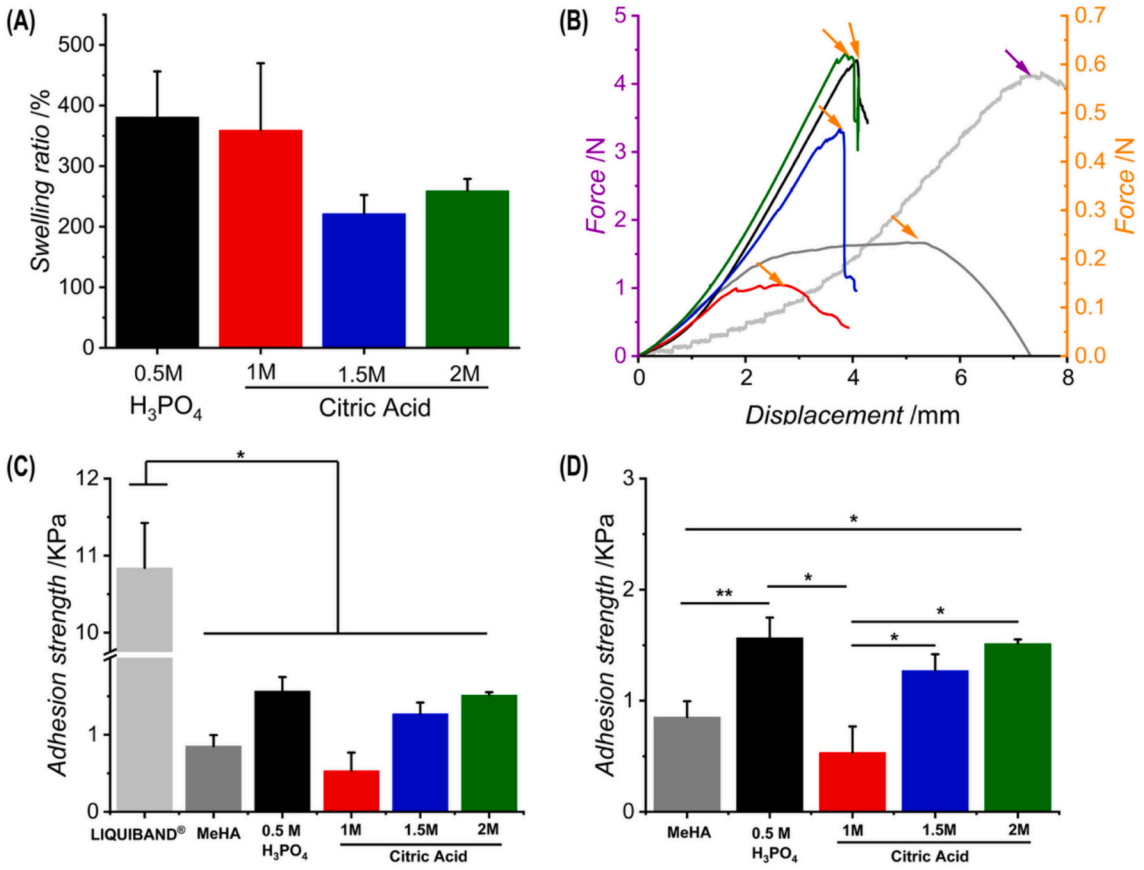

Fig. 9. Swelling, adhesion, and bonding performance of hydrogels. (A) Swelling ratios after 24 h in PBS. (B) Representative force–displacement curves recorded during porcine skin adhesion tests. Left axis: LIQUIBAND® only; right axis: all hydrogel groups. Light grey: LIQUIBAND®, grey: MeHA only, black: 0.5 M H_3PO_4; red: 1 M citric acid; blue: 1.5 M citric acid; green: 2 M citric acid. (C) Adhesion strength including LIQUIBAND® control. (D) Enlarged comparison of hydrogel groups.

Overall, the stronger adhesion achieved by the 1.5 M and 2 M citric acid-treated hydrogels correlated with their reduced swelling and more robust network structures. The more cohesive PEC-associated network structure likely enabled more stable interfacial contact under tensile loading, which is essential for firmly securing the hydrogel layer in cartilage repair settings where continuous hydration and mechanical stresses are unavoidable.

Following photo-crosslinking, the hydrogels were air-dried and subsequently treated overnight in 0.5 M NaOH to neutralise residual acidic components and assess alkaline stability. The morphological outcomes of this process are shown in Fig. 10A. The phosphoric-acid hydrogels in the top row underwent complete fragmentation after NaOH treatment, indicating poor structural resilience. In contrast, the citric acid-treated hydrogels demonstrated progressively enhanced stability with increasing acid concentration. The 1 M citric acid-treated hydrogel (red box) remained intact but did not recover its pre-drying morphology, whereas the 1.5 M sample (blue box) exhibited a more coherent structure after alkaline exposure. Notably, the 2 M citric acid-treated hydrogel almost fully restored its original shape, suggesting a resilient network capable of resisting both dehydration and NaOH exposure.

The compression behaviour of the NaOH-treated hydrogels (Fig. 10B) further supported these observations. The 2 M formulation, represented by the green curve, displayed a steep stress increase at low strain, consistent with a more cohesive and mechanically reinforced network. In contrast, the 1 M and 1.5 M formulations showed more compliant mechanical responses, reflected in slower stress build-up and lower maximum stresses. Together, these morphological and mechanical results suggest that citric acid contributes to concentration-dependent network reinforcement through carboxylate-associated ionic and hydrogen-bonding interactions, rather than acting solely as a passive acidic solvent. Such citrate-mediated secondary interactions, together with osmotic deswelling at high citric acid concentrations, likely contributed to the progressive increase in elastic modulus (Fig. 7B) and adhesion strength (Fig. 9C-D).

Importantly, the superior performance of citric acid-based networks aligns with the established benefits of citrate-based biomaterials. Modification of polymers with citric acid has been shown to endow antioxidant and anti-inflammatory properties, while the residual carboxyl and hydroxyl groups provide versatile sites for further functionalisation [10]. In citrate-based biomaterials, citric acid has been widely explored as a multifunctional component capable of contributing carboxyl- and hydroxyl-mediated interactions or crosslinking under appropriate reaction conditions. In the present system, the improved stability of CA-treated hydrogels is more conservatively attributed to citrate-mediated secondary interactions and PEC reinforcement.

Fig. 10C demonstrates the interfacial bonding behaviour of the hydrogels when applied to a 3D-printed scaffold. Following neutralisation in 0.5 M NaOH, air-drying on the scaffold, and subsequent rehydration in PBS, the 2 M citric-acid hydrogel remained firmly attached, retaining its structural integrity. In contrast, the H_3PO_4 hydrogel detached from the scaffold upon rehydration. These observations supported the mechanical findings and further suggested that citric-acid-induced network strengthening improved interfacial stability and resistance to detachment in aqueous environments relevant to biomedical applications.

To further support the chemical interpretation of the NaOH-induced recovery behaviour, ATR–FTIR spectra were collected from air-dried cured hydrogels before and after overnight treatment in 0.5 M NaOH, followed by direct air-drying (Fig. 11). Before NaOH treatment, the

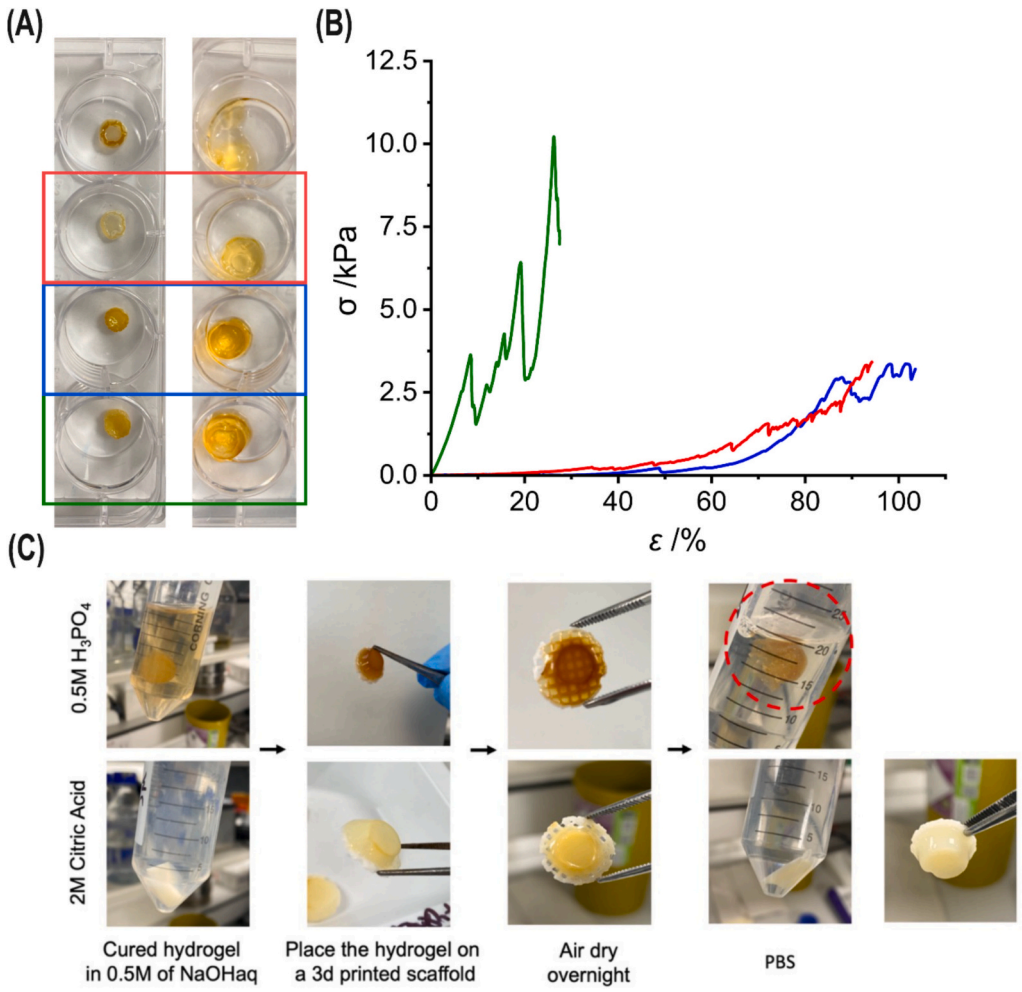

Fig. 10. Macroscopic appearance and mechanical performance of NaOH-treated hydrogels. (A) Photographs of air-dried hydrogels and samples after 0.5 M NaOH treatment. (B) Compression stress–strain curves of the corresponding hydrogels with schematic representation of the network-forming components. Colours: red (1 M citric acid), blue (1.5 M citric acid), green (2 M citric acid). (C) Bonding demonstration: 2 M citric acid hydrogel remained attached after rehydration; H_3PO_4 gel detached.

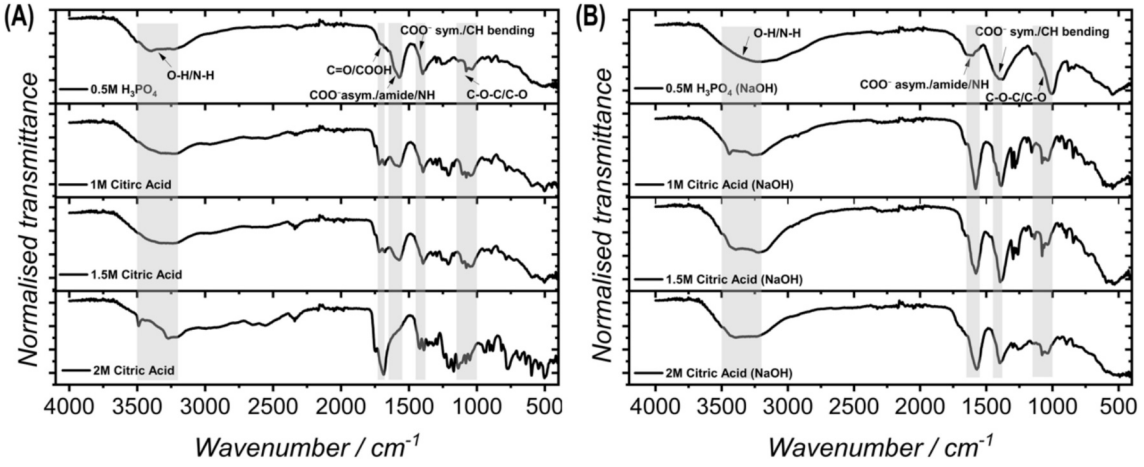

Fig. 11. ATR–FTIR analysis of hydrogels before and after NaOH exposure. (A) ATR–FTIR spectra of air-dried cured Cat–CS/MeHA hydrogels prepared with 0.5 M H_3PO_4 and 1–2 M citric acid before NaOH treatment. (B) Corresponding spectra after overnight exposure to 0.5 M NaOH followed by direct air-drying. Shaded regions indicate O–H/N–H, carbonyl/carboxylate, COO^-/amide and polysaccharide C–O–C/C–O bands. The spectral changes after NaOH exposure suggest carboxyl group deprotonation and carboxylate-associated ionic reorganisation, while retained polysaccharide bands indicate preservation of the Cat–CS/MeHA framework.

citric-acid-mediated hydrogels showed characteristic absorption in the O–H/N–H, carbonyl/carboxylate and polysaccharide backbone regions. After NaOH exposure, changes in the 1600–1550 cm^{-1} and 1450–1380 cm^{-1} regions became more evident, consistent with deprotonation of

carboxylic acid groups and reorganisation of sodium carboxylate-associated ionic environments. The retention of the C–O–C/C–O backbone region in the citric-acid-mediated hydrogels indicates preservation of the Cat–CS/MeHA framework after alkaline exposure. Because the samples were air-dried directly after NaOH treatment, the post-NaOH spectra are interpreted as reflecting the neutralised/alkaline-state hydrogel environment rather than a fully washed network. Together with the macroscopic recovery and compression results, these FTIR findings are consistent with a photo-crosslinked MeHA-based interpenetrating hydrogel network reinforced by Cat–CS/MeHA polyelectrolyte complexation and citrate-mediated secondary interactions.

3.5. Cytotoxicity analysis of hydrogels and their extracts

As the developed hydrogel is intended to function as a bioadhesive phase for osteochondral scaffold fabrication, cytocompatibility after neutralisation is an important requirement. The *in vitro* evaluation therefore focused on whether the neutralised hydrogels and their residual soluble components affected cell attachment, metabolic activity and viability. Three complementary assays were used: direct-contact Giemsa staining to assess cell morphology near the hydrogel surface, extract-based CCK-8 analysis to evaluate metabolic activity over time, and DAPI/Live-or-Dye™ staining to examine live/dead cell distribution during a 7-day culture period. Fig. 12A presents the Giemsa-stained images of L929 cells co-cultured with the hydrogels under different conditions. The top panel images compare untreated hydrogels with those subjected to 0.5 M NaOH neutralisation. The untreated hydrogel supported fewer adherent cells, and the surrounding cells exhibited a rounded and contracted morphology, indicating reduced attachment and limited spreading. In contrast, the NaOH-treated hydrogel displayed a substantially higher density of well-spread cells, suggesting that removal of residual acidic components created a more favourable microenvironment for cell adhesion.

Following NaOH treatment, the hydrogels supported cells that appeared morphologically normal, exhibiting elongated, well spread morphologies and uniform attachment across the surface. The absence of observable cellular abnormalities or localised degeneration suggests that the hydrogels did not exert detectable cytotoxic effects after the alkaline washing step, further suggesting that the cured Cat-CS/MeHA hydrogel networks are biocompatible, provided that residual acidic components are effectively removed.

Fig. 12B further supports the cytocompatibility of the materials using extract-based assays. When L929 cells were cultured in the presence of hydrogel extracts, the absorbance value, reflecting metabolic activity, increased markedly on days 3 and 5 relative to day 1. This progressive increase indicates sustained cell proliferation in the presence of the extracts and indicates that no detectable cytotoxic or growth-inhibitory effect was observed under the tested extract conditions. These data demonstrate that the citric acid-based hydrogels, once neutralised, showed no detectable cytotoxicity and supported cell growth under the tested conditions. It is important to emphasise that the extract-based assay evaluates the effect of leachable components rather than the bulk material itself; therefore, the absence of cytotoxicity suggests effective removal or neutralisation of residual acidic species and low release of harmful by-products. Therefore, subsequent scaffold-bonding and cytocompatibility interpretations were based on neutralised hydrogels rather than freshly cured acidic samples.

Fig. 13 presents the fluorescence staining results obtained using the DAPI and Live-or-Dye™ 594/614 assay over a 7-day culture period. Fig. 13A shows representative images provided by the staining kit to illustrate the assay's mode of action. DAPI permeates both viable and non-viable cells, staining all nuclei blue, whereas Live-or-Dye™ 594/614 selectively enters only cells with compromised membranes, labelling the nuclei of dead cells in red. When merged, viable cells appear blue, while non-viable cells appear purple due to the overlap of DAPI and the dead-cell dye. This staining was observed in the positive control, where the entire cell population was non-viable and thus displayed uniformly purple nuclei, and in the negative control, where only blue nuclear staining was visible, confirming the absence of dead cells.

Fig. 13B shows the merged staining outcomes for L929 cells cultured with hydrogel extracts from the different formulations at Days 1, 3, 5, and 7. At Day 1, all citric acid-based extracts resulted in predominantly blue nuclei with minimal red signal, indicating very low levels of acute cytotoxicity, while the phosphoric-acid extract exhibited slightly lower cell density but still exhibited only sparse dead-cell staining (Red). As the culture progressed to Days 3 and 5, the citric-acid groups,

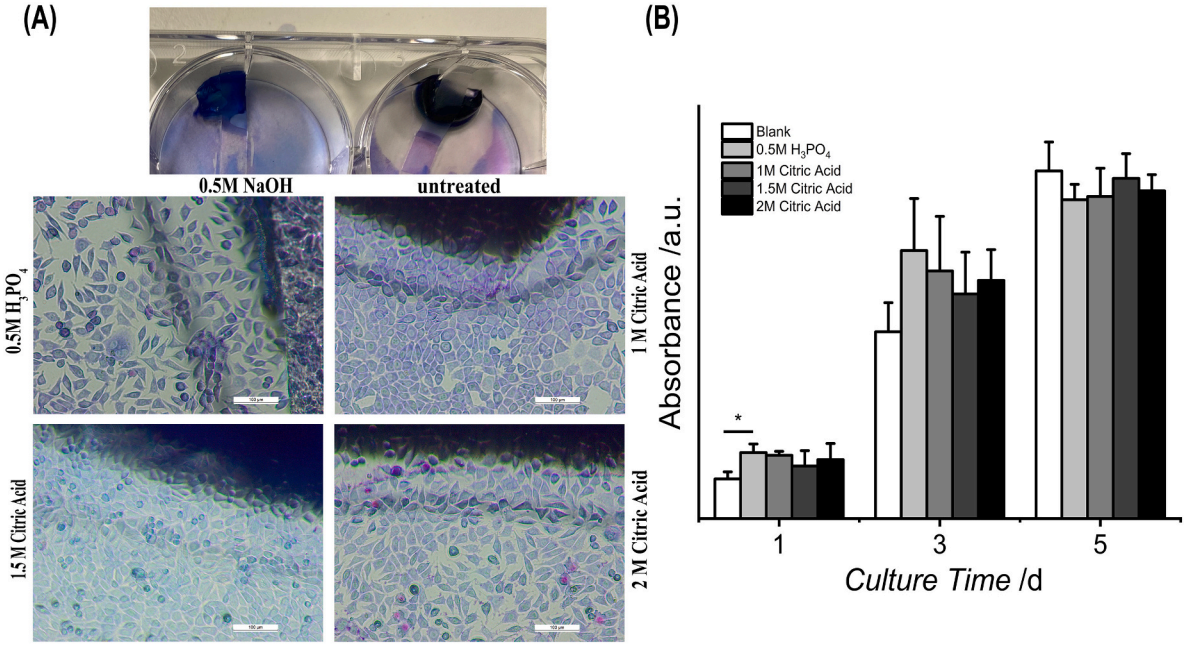

Fig. 12. Cytocompatibility assessment of hydrogels. (A) Giemsa-stained images of L929 cells cultured with untreated and NaOH-treated hydrogels, as well as hydrogels prepared using different acid systems. (B) Metabolic activity of L929 cells cultured with hydrogel extracts, showing increased absorbance at days 3 and 5 compared with day 1. Data represent mean ± SD (n=3). *$p < 0.05$.

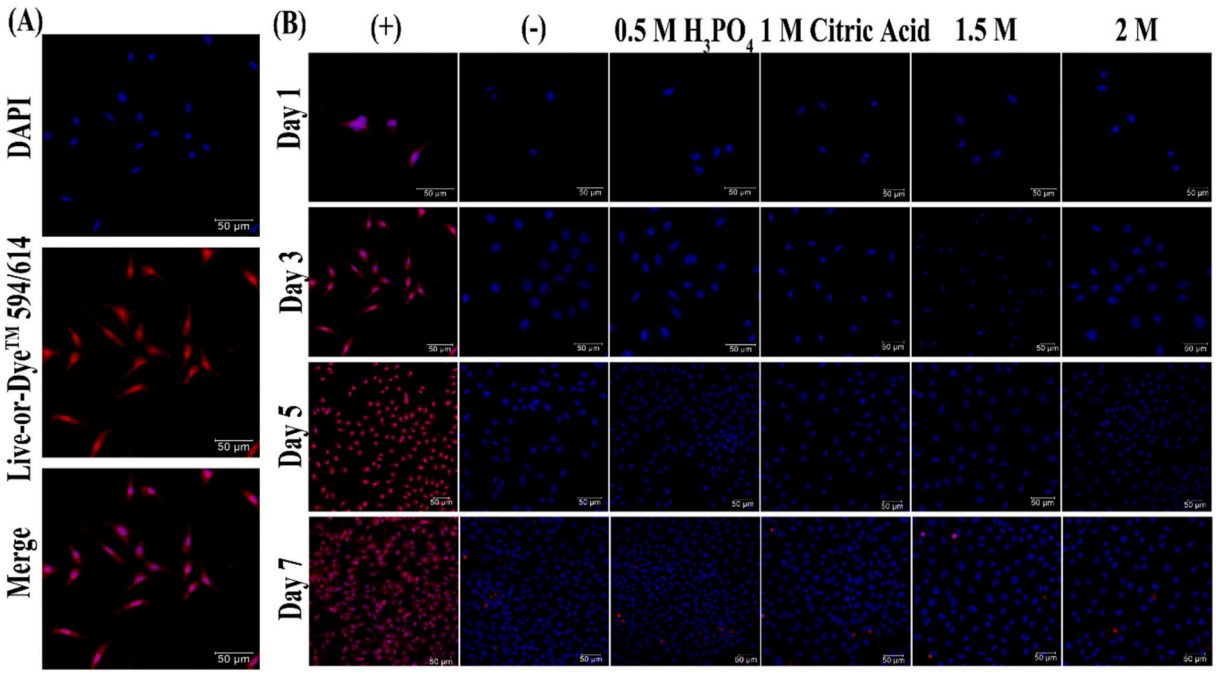

Fig. 13. Cell-viability analysis using DAPI and Live-or-Dye™ 594/614 staining. (A) Representative images illustrating assay function: DAPI labelling all cell nuclei and Live-or-Dye™ marking non-viable cells. (B) Fluorescence images (merge) of cells cultured with different hydrogel formulations for 1, 3, 5, and 7 days, indicating temporal changes in cell viability and morphology. The comparable predominance of viable cells among the neutralised hydrogel extract groups was used to confirm the absence of detectable formulation-dependent cytotoxicity, rather than to rank the formulations solely by cell viability.

particularly the 1.5 M and 2 M samples, supported increasing numbers of well-spread viable cells with negligible red staining, suggesting sustained cell compatibility. By Day 7, all extract groups, including the phosphoric-acid formulation, supported a dense layer of viable cells with exclusively blue nuclei and no detectable red signal. This suggests that none of the extract groups induced delayed cytotoxicity and that all hydrogels supported sustained cell proliferation under extract-based conditions.

Taken together, the DAPI/Live-or-Dye™ staining results indicate that extracts from the neutralised citric-acid-mediated hydrogels did not induce detectable acute or delayed cytotoxicity over the 7-day culture period. The predominance of DAPI-positive/Live-or-Dye-negative cells, together with the increasing cell density over time, supports the cytocompatibility of the neutralised hydrogel extracts. Although these assays do not demonstrate osteochondral tissue regeneration, they provide essential *in vitro* evidence that the developed hydrogel formulations are compatible with cell survival and proliferation under the tested conditions, supporting their further evaluation as adhesive interfacial layers in osteochondral scaffold fabrication.

The comparable viability observed among the neutralised hydrogel extracts should therefore be interpreted as a favourable safety outcome, indicating an absence of detectable formulation-dependent cytotoxicity rather than an absence of formulation-dependent material effects. The purpose of the cytocompatibility assessment was to determine whether the neutralised hydrogels caused detectable cytotoxicity, not to rank the formulations solely according to cell viability. Accordingly, the 2 M citric-acid formulation was identified as the most favourable group based primarily on its superior network stability, swelling resistance, mechanical reinforcement and scaffold-bonding performance, while the cytocompatibility results confirmed that these physicochemical improvements were not accompanied by compromised biological compatibility under the tested conditions.

4. Conclusion

This study developed a mussel-inspired, citric-acid-mediated Cat–CS/MeHA interpenetrating hydrogel network as a bioadhesive phase for osteochondral scaffold fabrication. Chemical characterisation confirmed the successful synthesis of methacrylated hyaluronic acid and catechol-functionalised chitosan, while solvent screening identified citric acid as a suitable biocompatible medium for homogeneous polymer dissolution and hydrogel formation. Among the tested formulations, the 2 M citric-acid hydrogel showed the most favourable overall performance, including improved network integrity, enhanced mechanical reinforcement, reduced swelling, stronger tissue adhesion and persistent wet bonding to a 3D-printed thermoplastic scaffold after rehydration.

These findings demonstrate that solvent acidity, particularly the use of multivalent citric acid, can serve as an effective formulation parameter for tuning PEC-based Cat–CS/MeHA hydrogel networks. Following neutralisation, the hydrogels supported fibroblast viability and proliferation, indicating good cytocompatibility under the tested conditions. Taken together, the resulting hydrogels combine mechanical stability, wet adhesion, short-term cyclic stability and cytocompatibility, supporting their potential use as interfacial bonding layers for integrated osteochondral scaffolds. Future studies should investigate gradient scaffold architectures, long-term dynamic loading responses, cell–material interactions in osteochondral-relevant models and *in vivo* performance to further validate this solvent-guided hydrogel strategy for integrated osteochondral scaffold development.

CRediT authorship contribution statement

Mingzu Du: Writing – original draft, Conceptualization. **Giuseppe Tronci:** Writing – review & editing, Supervision. **Xuebin B. Yang:** Writing – review & editing, Supervision. **Charles Brooker:** Writing – review & editing, Methodology. **David J. Wood:** Writing – review & editing, Supervision.

Funding

This work was supported by The University of Leeds-China Scholarship Council (CSC) Joint Scholarship (Grant No. 202206220017).

Declaration of competing interest

The authors declare no conflicts of interest.

Acknowledgements

The authors would like to thank Michael Brookes for his assistance with SEM characterisation, and Dr. Alex Heyam from the School of Chemistry for performing the NMR measurements.

Appendix A. Supplementary data

Supplementary data to this article can be found online at https://doi.org/10.1016/j.ijbiomac.2026.153122.

Data availability

Data will be made available on request.

References

[1] R.M.S. Pavel, A.L. Purza, D.M. Tit, A.-F. Radu, D.C. Iovanovici, D. Vasileva, B. Uivaraseanu, G. Bungau, C.D. Nistor-Cseppento, Functional burden and quality of life in hip and knee osteoarthritis: a cross-sectional study, Medicina 61 (7) (2025) 1155.
[2] E.H. Kim, S. Jeon, J. Park, J.H. Ryu, A. Mobasheri, C. Matta, E.-J. Jin, Progressing future osteoarthritis treatment toward precision medicine: integrating regenerative medicine, gene therapy and circadian biology, Exp. Mol. Med. 57 (6) (2025) 1133–1142.
[3] Q. Wang, W. Zhu, R. Wang, X. Weng, Hierarchical 3D-printed scaffolds for osteochondral regeneration: from biomimetic design to functional integration, Int. J. Bioprint. 11 (4) (2025) 4–31.
[4] J. Lu, Y. Gao, C. Cao, H. Wang, Y. Ruan, K. Qin, H. Liu, Y. Wang, P. Yang, Y. Liu, 3D bioprinted scaffolds for osteochondral regeneration: advancements and applications, Mater. Today Bio 32 (2025) 101834.
[5] M. Zhang, Q. Ye, Z. Zhu, S. Shi, C. Xu, R. Xie, Y. Li, Hyaluronic acid-based dynamic hydrogels for cartilage repair and regeneration, Gels 10 (11) (2024) 703.
[6] M. Li, F. Li, J. Xu, L. Zhu, J. Xiang, C. Zhu, Z. Dai, S. Tang, F. Ouyang, J. Yu, Bioadhesive chitosan hydrogel with dynamic covalent bonds and sustained kartogenin release for endogenous cartilage regeneration, Front. Bioeng. Biotechnol. 13 (2025) 1606726.
[7] G. Liu, X. Wei, Y. Zhai, J. Zhang, J. Li, Z. Zhao, T. Guan, D. Zhao, 3D printed osteochondral scaffolds: design strategies, present applications and future perspectives, Front. Bioeng. Biotechnol. 12 (2024) 1339916.
[8] S. Kadyr, B. Khumyrzakh, S. Naz, A. Abdossova, B. Askarbek, D.M. Kalyon, Z. Liu, C. Erisken, Hydrogels for osteochondral interface regeneration: biomaterial types, processes, and animal models, Gels 12 (1) (2025) 24.
[9] S. Zhang, C. Liu, M. Su, D. Zhou, Z. Tao, S. Wu, L. Xiao, Y. Li, Development of citric acid-based biomaterials for biomedical applications, J. Mater. Chem. B 12 (45) (2024) 11611–11635.
[10] H. Xu, S. Yan, E. Gerhard, D. Xie, X. Liu, B. Zhang, D. Shi, G.A. Ameer, J. Yang, Citric acid: a nexus between cellular mechanisms and biomaterial innovations, Adv. Mater. 36 (32) (2024) 2402871.
[11] J.H. Ryu, S. Hong, H. Lee, Bio-inspired adhesive catechol-conjugated chitosan for biomedical applications: a mini review, Acta Biomater. 27 (2015) 101–115.
[12] Z. Wang, X. Wan, S. Wang, Bioinspired chemical design to control interfacial wet adhesion, Chem 9 (4) (2023) 771–783.
[13] A. Kayitmazer, A. Koksal, E.K. Iyilik, Complex coacervation of hyaluronic acid and chitosan: effects of pH, ionic strength, charge density, chain length and the charge ratio, Soft Matter 11 (44) (2015) 8605–8612.
[14] A. Bonaccorso, E. Zingale, C. Carbone, T. Musumeci, R. Pignatello, A current overview of polyions and polyelectrolyte complexes for pharmaceutical applications with special emphasis to brain purposes, J. Pharm. Investig. (2025) 1–29.
[15] F. Hong, P. Qiu, Y. Wang, P. Ren, J. Liu, J. Zhao, D. Gou, Chitosan-based hydrogels: from preparation to applications, a review, Food Chem. X 21 (2024) 101095.
[16] N. Sharmin, J.T. Rosnes, L. Prabhu, U. Böcker, M. Sivertsvik, Effect of citric acid cross linking on the mechanical, rheological and barrier properties of chitosan, Molecules 27 (16) (2022) 5118.
[17] M. Hamdine, M.-C. Heuzey, A. Bégin, Viscoelastic properties of phosphoric and oxalic acid-based chitosan hydrogels, Rheol. Acta 45 (5) (2006) 659–675.
[18] B. Zhao, M. Zhao, H. Sun, Y. Yang, S. Sun, H. Yu, M. He, Y. Sun, Y. Cheng, Preparation and characterization of photo-oxidative dual-crosslinked chitosan/hyaluronic acid hydrogels, React. Funct. Polym. 180 (2022) 105378.
[19] G. Conejo-Cuevas, L. Ruiz-Rubio, V. Sáez-Martínez, R. Pérez-González, O. Gartziandia, A. Huguet-Casquero, L. Pérez-Álvarez, Spontaneous gelation of adhesive catechol modified hyaluronic acid and chitosan, Polymers 14 (6) (2022) 1209.
[20] S. Zhou, Z. Bei, J. Wei, X. Yan, H. Wen, Y. Cao, H. Li, Mussel-inspired injectable chitosan hydrogel modified with catechol for cell adhesion and cartilage defect repair, J. Mater. Chem. B 10 (7) (2022) 1019–1030.
[21] J. Yang, A. Duan, L. Shen, Q. Liu, F. Wang, Y. Liu, Preparation and application of curcumin loaded with citric acid crosslinked chitosan-gelatin hydrogels, Int. J. Biol. Macromol. 264 (2024) 130801.
[22] A.R. Narkar, E. Cannon, H. Yildirim-Alicea, K. Ahn, Catechol-functionalized chitosan: optimized preparation method and its interaction with mucin, Langmuir 35 (48) (2019) 16013–16023.
[23] T.B. Ngo, B.S. Spearman, N. Hlavac, C.E. Schmidt, Three-dimensional bioprinted hyaluronic acid hydrogel test beds for assessing neural cell responses to competitive growth stimuli, ACS Biomater. Sci. Eng. 6 (12) (2020) 6819–6830.
[24] H. Montazerian, S. Mitra, A. Hassani Najafabadi, R. Seyedmahmoud, Y. Zheng, M. R. Dokmeci, N. Annabi, A. Khademhosseini, P.S. Weiss, Catechol conjugation for bioadhesion in photo-cross-linkable biomaterials, ACS Mater. Lett. 5 (6) (2023) 1672–1683.
[25] R. Zhang, C. Brooker, L.L. Whitehouse, N.H. Thomson, D. Wood, G. Tronci, Mechanical and suture-holding properties of a UV-cured atelocollagen membrane with varied crosslinked architecture, Biomed. Mater. 19 (6) (2024) 065036.
[26] C. Brooker, G. Tronci, Effect of mammalian tissue source on the molecular and macroscopic characteristics of UV-cured type I collagen hydrogel networks, Prosthesis 4 (1) (2022) 1–14.
[27] Z. Gao, X. Yang, E. Jones, P.A. Bingham, A. Scrimshire, P.D. Thornton, G. Tronci, An injectable, self-healing and MMP-inhibiting hyaluronic acid gel via iron coordination, Int. J. Biol. Macromol. 165 (2020) 2022–2029.
[28] H. Liang, J. Yin, K. Man, X.B. Yang, E. Calciolari, N. Donos, S.J. Russell, D.J. Wood, G. Tronci, A long-lasting guided bone regeneration membrane from sequentially functionalised photoactive atelocollagen, Acta Biomater. 140 (2022) 190–205.
[29] H. Liang, S.J. Russell, D.J. Wood, G. Tronci, Monomer-induced customization of UV-cured atelocollagen hydrogel networks, Front. Chem. 6 (2018) 626.
[30] R. Holmes, X.B. Yang, A. Dunne, L. Florea, D. Wood, G. Tronci, Thiol-ene photo-click collagen-PEG hydrogels: impact of water-soluble photoinitiators on cell viability, gelation kinetics and rheological properties, Polymers 9 (6) (2017) 226.
[31] W. Han, B. Zhou, K. Yang, X. Xiong, S. Luan, Y. Wang, Z. Xu, P. Lei, Z. Luo, J. Gao, Biofilm-inspired adhesive and antibacterial hydrogel with tough tissue integration performance for sealing hemostasis and wound healing, Bioact. Mater. 5 (4) (2020) 768–778.
[32] Y. Xing, X. Qing, H. Xia, S. Hao, H. Zhu, Y. He, H. Mao, Z. Gu, Injectable hydrogel based on modified gelatin and sodium alginate for soft-tissue adhesive, Front. Chem. 9 (2021) 744099.
[33] C. Buckley, T.R. Montgomery, T. Szank, B.A. Murray, C. Quigley, I. Major, Modification of hyaluronic acid to enable click chemistry photo-crosslinking of hydrogels with tailorable degradation profiles, Int. J. Biol. Macromol. 240 (2023) 124459.
[34] G. Tronci, H. Ajiro, S.J. Russell, D.J. Wood, M. Akashi, Tunable drug-loading capability of chitosan hydrogels with varied network architectures, Acta Biomater. 10 (2) (2014) 821–830.
[35] M. Li, C. Brooker, R. Ambike, Z. Gao, P. Thornton, T. Do, G. Tronci, Photodynamic, UV-curable and fibre-forming polyvinyl alcohol derivative with broad processability and staining-free antibacterial capability, Eur. Polym. J. 228 (2025) 113794.
[36] G. Tronci, C.A. Grant, N.H. Thomson, S.J. Russell, D.J. Wood, Multi-scale mechanical characterization of highly swollen photo-activated collagen hydrogels, J. R. Soc. Interface 12 (102) (2015).
[37] G. Tronci, S.J. Russell, D.J. Wood, Photo-active collagen systems with controlled triple helix architecture, J. Mater. Chem. B 1 (30) (2013) 3705–3715.
[38] T.N. Snyder, K. Madhavan, M. Intrator, R.C. Dregalla, D. Park, A fibrin/hyaluronic acid hydrogel for the delivery of mesenchymal stem cells and potential for articular cartilage repair, J. Biol. Eng. 8 (1) (2014) 10.
[39] Y.-T. Lan, Q.-P. Cheng, J. Xu, S.-H. Lin, J.-M. Lin, S.-h. Hsu, Gelation and the self-healing behavior of the chitosan–catechol hydrogel, Polymers 14 (21) (2022) 4614.
[40] A. Scalzone, M.A. Bonifacio, S. Cometa, F. Cucinotta, E. De Giglio, A.M. Ferreira, P. Gentile, pH-triggered adhesiveness and cohesiveness of chondroitin sulfate-catechol biopolymer for biomedical applications, Front. Bioeng. Biotechnol. 8 (2020) 712.
[41] L.E. Arnow, Colorimetric determination of the components of 3, 4-dihydroxyphenylalanine-tyrosine mixtures, J. Biol. Chem. 118 (2) (1937) 531–537.
[42] R. Pinnataip, B.P. Lee, Oxidation chemistry of catechol utilized in designing stimuli-responsive adhesives and antipathogenic biomaterials, ACS Omega 6 (8) (2021) 5113–5118.
[43] M. Lucarini, G.F. Pedulli, M. Guerra, A critical evaluation of the factors determining the effect of intramolecular hydrogen bonding on the O H bond dissociation enthalpy of catechol and of flavonoid antioxidants, Chem. Eur. J. 10 (4) (2004) 933–939.
[44] S. Patel, S. Sharma, J. Suthar, M. Suryawanshi, Regulatory Concern for Biomaterial and its Toxicity, in: Design and Processing of Green Materials, Springer, 2025, pp. 433–458.
[45] V.R. Askari, H.S. Roudi, M.S. Fadaei, R. Safaei, M. Boroomand, M.M. Dabbaghi, V. B. Rahimi, Regulatory Considerations of Natural Biopolymers for Drug Delivery, in: Natural Biopolymers for Drug Delivery, Elsevier, 2025, pp. 747–767.
[46] R. Karpiński, A. Prus, J. Baj, S. Radej, M. Prządka, P. Krakowski, K. Jonak, Articular cartilage: structure, biomechanics, and the potential of conventional and advanced diagnostics, Appl. Sci. 15 (12) (2025) 6896.
[47] S. Çitoğlu, H. Duran, Recent advances in porous nanomaterials-based drug delivery systems for osteoarthritis, Nano Select 5 (7–8) (2024) 2300099.

[48] Y. Xiang, J. Yan, X. Bao, A. Gleadall, T. Sun, Investigation of cell infiltration and colonization in 3D porous scaffolds via integrated experimental and computational strategies, J. Biotechnol. 382 (2024) 78–87.
[49] F. Mukasheva, L. Adilova, A. Dyussenbinov, B. Yernaimanova, M. Abilev, D. Akilbekova, Optimizing scaffold pore size for tissue engineering: insights across various tissue types, Front. Bioeng. Biotechnol. 12 (2024) 1444986.
[50] B. Zheng, J. Xing, X. Tang, Z. He, Q. Tang, S. Liu, Y. Xiao, J. Xu, E. Luo, Y. Liu, Tailored surface topographical scaffolds: a breakthrough in osteoarthritic cartilage and subchondral bone defect repair, J. Mater. Chem. B 13 (2025) 8639–8652.
[51] Y. Li, L. Ji, J. Yu, F. Zhu, Y. Xiang, X. Wang, J. Wang, C. Liu, Bioactive materials-mediated regulation of bone marrow microenvironment: mechanistic insights and therapeutic potentials, Adv. Mater. 38 (1) (2026) e11497.
[52] Z. Gao, L. Hassouneh, X. Yang, J. Pang, P.D. Thornton, G. Tronci, Hydrogen phosphate-mediated acellular biomineralisation within a dual crosslinked hyaluronic acid hydrogel, Eur. Polym. J. 143 (2021) 110187.